

# **ADDITIVE MANUFACTURING OF INCONEL 617 SUPERALLOY BY LAM-DED AND WAAM AND ITS IN-SITU MONITORING**

**M.Tech. Thesis**

By  
**HIMANSHU SHARMA**  
**2302103018**



**DEPARTMENT OF MECHANICAL ENGINEERING**  
**INDIAN INSTITUTE OF TECHNOLOGY INDORE**

**MAY 2025**



# **ADDITIVE MANUFACTURING OF INCONEL 617 SUPERALLOY BY LAM-DED AND WAAM AND ITS IN-SITU MONITORING**

**A THESIS**

*Submitted in partial fulfillment of the  
requirements for the award of the degree*

*of*

**Master of Technology**

*by*

**HIMANSHU SHARMA**

**2302103018**



**DEPARTMENT OF MECHANICAL ENGINEERING**

**INDIAN INSTITUTE OF TECHNOLOGY INDORE**

**MAY 2025**






# INDIAN INSTITUTE OF TECHNOLOGY INDORE

## CANDIDATE'S DECLARATION

I hereby certify that the work which is being presented in the thesis entitled “**ADDITIVE MANUFACTURING OF INCONEL 617 SUPERALLOY BY LAM-DED AND WAAM AND ITS IN-SITU MONITORING**” in the partial fulfillment of the requirements for the award of the degree of **MASTER OF TECHNOLOGY** and submitted in the **DEPARTMENT OF MECHANICAL ENGINEERING, Indian Institute of Technology Indore**, is an authentic record of my own work carried out during the time period from July 2023 to May 2025 under the supervision of Dr. I. A. Palani, Professor, Department of Mechanical Engineering, Indian Institute of Technology, Indore and Dr. C. P. Paul, SOH, Head, EDMD, Raja Ramanna Centre for Advanced Technology, Indore. The matter presented in this thesis has not been submitted by me for the award of any other degree of this or any other institute.

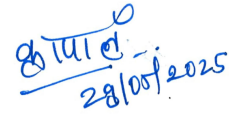
  
28/5/25.

Signature of the student with date  
(HIMANSHU SHARMA)

-----  
This is to certify that the above statement made by the candidate is correct to the best of my/our knowledge.

  
28th/5/2025

Signature of the Supervisor of  
M.Tech. thesis #1 (with date)  
(Prof. I. A. Palani)

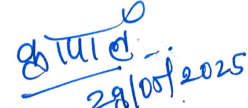
  
28/05/2025

Signature of the Supervisor of  
M.Tech. thesis #2 (with date)  
(Dr. C. P. Paul)

-----  
**HIMANSHU SHARMA** has successfully given his/her M.Tech. Oral Examination held on **09.05.2025**.

  
28th/5/2025

Signature of Supervisor of M.Tech. thesis #1  
Date:

  
28/05/2025

Signature of Supervisor of M.Tech. thesis #2  
Date:



Convener, DPGC  
Date: 29-05-2025

## ACKNOWLEDGEMENTS

It would not have been possible for me to prepare my master's thesis without the help, guidance, and support of some wonderful people, who shaped my ideas and helped in my research during the tenure of Master of Technology.

First and foremost, I would like to extend my sincere gratitude to my research supervisors, **Prof. I. A. Palani** and **Prof. C. P. Paul** for their invaluable guidance, continuous support, and encouragement throughout the course of this research. They have significantly influenced my intellectual and personal growth during this important phase of my life. Their profound knowledge, insightful suggestions, and constructive feedback have played a vital role in shaping this work. Their stimulating discussions and constructive criticisms have put me always on my toes, playing a pivotal role in shaping my research journey. Their patience, motivation, and mentorship have not only helped me grow as a researcher but have also inspired me to pursue excellence in the field. It has been a privilege to work under their guidance, and I will always remain grateful for their contribution to this work and to my academic journey.

My special thanks to **Prof. Suhas S. Joshi**, Director, IIT Indore, **Shri Unmesh D. Malshe**, Director, Raja Ramanna Centre for Advanced Technology (RRCAT), Indore and **Dr. Shanmugan Dhinakaran**, Head of Department, Mechanical Engineering, IIT Indore, for supporting me with sophisticated facilities to conduct my research. I extend my sincere thanks to the DPGC Convenor, **Dr. S. Janakiraman**, for the constant support. I extend my sincere thanks to **Ministry of Education (MoE)**, Government of India for funding me from July 2023 to May 2025. I deeply express my thanks to the **Department of Mechanical Engineering, IIT Indore, Department of MEMS, IIT Indore** and **Sophisticated Instrumentation Centre, IIT Indore** for allowing access to the facility of various characterization techniques.

I take this opportunity to express my thanks to my very special seniors, **Dr. Anshu Sahu, Dr. Sunil Yadav** and **Mr. Arpit Kumar Singh** for their brotherly help and giving me moral support during my research journey at IIT Indore and RRCAT.

I sincerely express my thanks to the brilliant minds of Mechatronics and Instrumentation Laboratory, **Dr. Nandini Patra, Dr. Kaushal Gangwar, Mr. Nikunj Bheda** and **Ms. Diksha Jaurker** for their constant support. Also, I would like to thank my junior fellows in the lab. I extend my cordial thanks to **Mr. Ashwin Wagh** and **Mr. Krishnpal Singh Tomar** for their kind cooperation and support.

Good friends are like anchors during turbulent times and companions in moments of joy. Their presence makes the challenging moments more bearable and the accomplishments more joyful. I have been truly fortunate to have such friends beside me during my M. Tech journey. I take this stage to thank my batchmates and friends, **Himanshu, Rushikesh, Pallvi, Abneesh** and **Vivek**. Your encouragement and companionship have been invaluable. Thank you for being part of this journey and making it memorable in every way.

All this wouldn't have been possible without the unwavering love, sacrifice, support and their countless blessings. My parents, **Shri. Hemendra Prasad Sharma** and **Smt. Hemlata Sharma** have always been a source of inspiration for me as well as a source of motivation for all my good work in my life. My brother **Harshit** has always been my motivation and friend of my all-odd times in my life. Your constant support, both emotionally and morally, has been the foundation of everything I have achieved.

**"Heartfelt thanks to all of you for making this journey truly memorable."**

*(Himanshu Sharma)*

***DEDICATED TO MY  
BELOVED FAMILY AND MY  
RESPECTED TEACHERS!***



## ABSTRACT

Additive Manufacturing (AM) has emerged as a transformative technology for producing intricate, high-performance components, notably in the aerospace and energy production sector, where materials must withstand extreme environmental conditions. Inconel 617, which primarily consists of Nickel, Chromium, Cobalt and Chromium is a Ni-based superalloy, which is very well suited for such demanding applications due to its exceptional high temperature strength, oxidation and corrosion resistance at elevated temperatures. However, manufacturing of In-617 through conventional methods remains a challenge due to the various problems associated with it such as poor machinability,  $\sigma$ -Phase Precipitation, tendency of thermal cracking and various machining difficulties such as rapid tool degradation and work hardening.

The present study explores the fabrication of Inconel 617 using two prominent Directed Energy Deposition (DED) - based AM techniques: Laser Additive Manufacturing - Directed Energy Deposition (LAM-DED) and Wire Arc Additive Manufacturing (WAAM), with a particular emphasis on in-situ process monitoring. This study focuses on the Realization of In-617 in Additive manufacturing route for catering heavy industries, particularly the energy production sectors. Preliminary investigations were conducted using LAM-DED to assess laser-material interactions and understand basic melt pool characteristics. Single track deposition followed by the bulk deposition was performed and the microstructural analysis and mechanical tests were conducted. While LAM - DED allows for high precision and better control of microstructural features, it has some disadvantages associated with it, such as low deposition rates, higher costs, material wastage as well as challenges associated with the powder handling.

To address these limitations, the research transitioned to WAAM, which offers higher deposition rates, improved material utilization, and lower operational costs by using wire feedstock. Parameters were optimized for single track deposition by varying the operating parameters, i.e. voltage, wire feed rate and deposition speed. On the optimized parameter, bulk deposition was carried out using two different scanning strategies. Extensive

characterization—including microstructural analysis, microhardness testing, tensile stress evaluations, XRD analysis and residual stress calculations were performed on the fabricated specimens.

A major novelty of this work lies in the development and integration of an in-situ monitoring technique based on Time Resolved Reflectivity (TRR) within the WAAM setup. This technique enables real time behavior of melt pool by analyzing the fluctuations in reflection intensity. The system was also employed in discontinuity detection during the WAAM deposition. It could serve as a valuable tool for quality monitoring and a closed loop feedback system.

In summary, this study validates WAAM as a viable technique for manufacturing Inconel 617 components and introduces a novel approach for real-time process monitoring. The findings contribute to advancing reliable and cost-effective AM processes for high-temperature structural alloy.

## LIST OF PUBLICATIONS

### Conference Publications:

- [1] **Himanshu Sharma**, S Yadav, CP Paul, I A Palani “Investigations on Mechanical Properties and Microstructural Analysis of Inconel-617 deposited by Powder-Fed LAM-DED” 2024, International Conference on Precision, Meso, Micro and Nano Engineering (COPEN) – **Accepted for conference proceedings**
- [2] **Himanshu Sharma**, Anshu Sahu, CP Paul, I A Palani “Investigations on characteristics of Inconel 617 superalloy fabricated by wire arc additive manufacturing.” - IMECE-ASME-2025 – **Accepted for conference proceedings**
- [3] **Himanshu Sharma**, CP Paul, I A Palani “Evaluating the Effects of Laser Nitriding on NiTi Shape Memory Alloy fabricated by Wire Arc Additive Manufacturing.”-National Laser Symposium-33 – **Accepted for proceedings**
- [4] **Himanshu Sharma**, Naveen Kumar, Rushikesh A Mali, I A Palani “Investigation of Laser process parameters on Laser Surface Hardening using Nanosecond Pulsed Nd: YAG Laser.” - National Laser Symposium-32 – **NLS – 32 Proceedings**

# **TABLE OF CONTENTS**

<b>LIST OF FIGURES</b>	<b>15-18</b>
<b>LIST OF TABLES</b>	<b>19</b>
<b>ACRONYMS</b>	<b>20</b>

<b>Chapter 1: Introduction</b>	<b>22-35</b>
1.1 Additive Manufacturing	22-27
1.1.1 Classification of Additive Manufacturing	22-24
1.1.2 Laser Additive Manufacturing-Directed Energy Deposition (LAM-DED)	24-25
1.1.3 Wire Arc Additive Manufacturing (WAAM)	25-27
1.2 In-situ Monitoring	27-30
1.2.1 Various Monitoring Techniques in AM	27-29
1.2.2 Time Resolved Reflectivity (TRR)	29-30
1.3 Motivation of the Present Study	30-34
1.3.1 High-Temperature Thermal Power Plants: The Need of the Day	30-32
1.3.2 Alloy 617: The Backbone of Indian Advanced Ultra-Supercritical Thermal Power Plant Program	32-34
1.4 Research Objectives	34
1.5 Structure of the Thesis	35
<b>Chapter 2: Literature Survey</b>	<b>36-43</b>
2.1 Current status on Additive Manufacturing of Inconel 617 superalloy	36-40
2.1.1 LAM – DED	37-38
2.1.2 WAAM	38-40

<b>2.2 Need for Real time monitoring in Additive Manufacturing</b>	<b>40-43</b>
<b>Chapter 3: Materials, Methods and Characterization Techniques</b>	<b>44-55</b>
<b>3.1 Material Specifications</b>	<b>44-45</b>
<b>3.2 Material challenges related to Inconel 617</b>	<b>45-46</b>
<b>3.3 Experimental Setups</b>	<b>46-50</b>
3.3.1 Laser Additive Manufacturing-Directed Energy Deposition (LAM-DED)	<b>47-48</b>
3.3.2 Wire Arc Additive Manufacturing (WAAM)	<b>48-49</b>
3.3.3 Time Resolved Reflectivity (TRR)	<b>49-50</b>
<b>3.4 Material Characterization</b>	<b>51-54</b>
3.4.1 Metallographic Characterization	<b>51</b>
3.4.2 Field Emission Scanning Electron Microscopy (FESEM)	<b>52</b>
3.4.3 Energy Dispersive Spectroscopy (EDS)	<b>53</b>
3.4.4 X - Ray Diffraction (XRD)	<b>54</b>
<b>3.5 Mechanical Testing</b>	<b>54-55</b>
3.5.1 Micro Hardness Test	<b>54-55</b>
3.5.2 Tensile Test	<b>55</b>
<b>Chapter 4: Experimental Investigations on Additive Manufacturing of Inconel 617 Superalloy</b>	<b>56-85</b>
<b>4.1 Preliminary Experiments using LAM-DED</b>	<b>56-62</b>
4.1.1 Single Track Analysis	<b>57-58</b>
4.1.2 Bulk Deposition	<b>58-59</b>
4.1.3 Microstructural Analysis	<b>59-60</b>
4.1.4 Microhardness Test	<b>60-61</b>
4.1.5 Tensile Properties	<b>61-62</b>
<b>4.2 WAAM Analysis</b>	<b>62-64</b>
4.2.1 Pilot experiments to optimize the process parameters	<b>63</b>
4.2.2 Deposition parameters for WAAM	<b>63</b>
4.2.3 Development of Taguchi's L-9 model for WAAM deposition	<b>64</b>

<b>4.3 Single Track Analysis</b>	<b>64-70</b>
4.3.1 ANOVA Analysis	<b>66-68</b>
4.3.1.1 Effect of voltage, wire feed rate, and deposition speed on track width	<b>66-67</b>
4.3.1.2 Effect of voltage, wire feed rate, and deposition speed on track height	<b>67-68</b>
4.3.2 Microstructural Analysis	<b>68-69</b>
4.3.3 Microhardness Analysis	<b>70</b>
<b>4.4 Bulk Deposition</b>	<b>70-81</b>
4.4.1 Microstructural Analysis	<b>71</b>
4.4.1.1 Bidirectional Deposition Strategy	<b>72</b>
4.4.1.2 Unidirectional Deposition Strategy	<b>72-73</b>
4.4.2 Microhardness Analysis	<b>74-75</b>
4.4.3 Tensile Test	<b>75-79</b>
4.4.4 XRD Analysis	<b>79-80</b>
4.4.5 Residual Stress Analysis	<b>80-81</b>
<b>4.5 In-situ Monitoring of WAAM Deposition</b>	<b>81-85</b>
4.5.1 Discontinuity detection using TRR	<b>83-85</b>
<b>Chapter 5: Conclusions and Future Scope</b>	<b>86-89</b>
<b>5.1 Conclusions</b>	<b>86-88</b>
<b>5.2 Future Scope</b>	<b>89</b>
 <b>REFERENCES</b>	 <b>90-93</b>

## LIST OF FIGURES

<b>Fig. 1.1</b>	Types of Additive Manufacturing Processes
<b>Fig. 1.2</b>	Powder feeding methods in LAM-DED, (a) Coaxial and (b) Off-axis
<b>Fig. 1.3</b>	Different WAAM Techniques; (a) GMAW, (b) GTAW and (c) PAW
<b>Fig. 1.4</b>	Schematic of TRR Setup
<b>Fig. 1.5</b>	Indicative CO <sub>2</sub> emission reduction pathways
<b>Fig. 1.6</b>	Progress of various thermal power plants
<b>Fig. 1.7</b>	Outlet header used in thermal power plants
<b>Fig. 1.8</b>	Plan of work
<b>Fig. 2.1</b>	Effect of laser power and scan speed on track height(left) & track width(right)
<b>Fig. 2.2</b>	Optical micrographs of the as-deposited In-617 wall at different locations along the building direction
<b>Fig. 2.3</b>	Analysis of grain growth
<b>Fig. 2.4</b>	Real-time measurements of the melt pool width and length using coaxial IR camera
<b>Fig. 2.5</b>	Melt pool depth estimation system for DED process
<b>Fig. 2.6</b>	Structure diagram of LQR control system based on PSO
<b>Fig. 2.7</b>	Image processing steps to obtain the melt pool width
<b>Fig. 2.8</b>	Temperature feedback loop
<b>Fig. 3.1</b>	5-axis LAM-DED developed at RRCAT
<b>Fig. 3.2</b>	Schematic of the LAM-DED setup
<b>Fig. 3.3</b>	Pictorial view of WAAM setup
<b>Fig. 3.4</b>	Schematic of the WAAM setup
<b>Fig. 3.5</b>	2-D drawing of TRR setup
<b>Fig. 3.6</b>	Schematic of TRR setup

<b>Fig. 3.7</b>	TRR setup implemented on WAAM
<b>Fig. 3.8</b>	Polishing Machine
<b>Fig. 3.9</b>	Field Emission Scanning Electron Microscopy (FESEM)
<b>Fig. 3.10</b>	X-ray diffractometer using Cu-K $\alpha$ radiations
<b>Fig. 3.11</b>	Bragg's Law in a 2-D crystal
<b>Fig. 3.12</b>	Vickers microhardness test setup
<b>Fig. 3.13</b>	Universal testing machine (left) and 2-D drawing for micro-tensile sample(right)
<b>Fig. 4.1</b>	Pilot experiments done for parameter optimization
<b>Fig. 4.2</b>	Single track deposition at optimized parameters
<b>Fig. 4.3</b>	Deposited block using LAM-DED
<b>Fig. 4.4</b>	(a)Formation of cellular and equiaxed grains in bottom layer;(b) Initialization of columnar grains in the upper layers;(c) Layer band formation;(d) Inter-dendritic segregations
<b>Fig. 4.5</b>	(a)Indentations on a single layer;(b) Microhardness value variations at different layers
<b>Fig. 4.6</b>	(a)Tensile test specimen;(b) Stress-Strain curve for the specimens
<b>Fig. 4.7</b>	Pilot experiments for optimizing the process parameters of WAAM
<b>Fig. 4.8</b>	Schematic for the track geometry analysis
<b>Fig. 4.9</b>	Single track deposition at various parameters
<b>Fig. 4.10</b>	Track geometry analysis
<b>Fig. 4.11</b>	Main Effects plot for track width
<b>Fig. 4.12</b>	Interaction plots for track width
<b>Fig. 4.13</b>	Main Effects plot for track height
<b>Fig. 4.14</b>	Interaction plots for track height
<b>Fig. 4.15</b>	Cutting of single tracks and sample preparation for microstructural analysis



<b>Fig. 4.16</b>	Microstructure of the selected tracks
<b>Fig. 4.17</b>	Grain size variation at selected parameters
<b>Fig. 4.18</b>	Microhardness variation at selected parameters
<b>Fig. 4.19</b>	Bidirectional deposition strategy schematic(left) and deposited wall(right)
<b>Fig. 4.20</b>	Unidirectional deposition strategy schematic(left) and deposited wall(right)
<b>Fig. 4.21</b>	Microstructure variation across layers in bidirectional strategy
<b>Fig. 4.22</b>	Microstructure variation across layers in unidirectional strategy
<b>Fig. 4.23</b>	Grain size variation across layers in (a) bidirectional strategy and (b) unidirectional strategy
<b>Fig. 4.24</b>	Microhardness variation in in (a) bidirectional strategy and (b) unidirectional strategy
<b>Fig. 4.25</b>	Schematic for micro tensile test
<b>Fig. 4.26</b>	Tensile test results for bidirectional deposition; (a) horizontal orientation and (b) vertical orientation
<b>Fig. 4.27</b>	Tensile test results for unidirectional deposition; (a) horizontal orientation and (b) vertical orientation
<b>Fig. 4.28</b>	Fractography images for; (a) horizontally oriented specimen using bidirectional strategy, (b) vertically oriented specimen using bidirectional strategy, (c) horizontally oriented specimen using unidirectional strategy, (d) vertically oriented specimen using unidirectional strategy
<b>Fig. 4.29</b>	XRD patterns for WAAM deposited In-617; (a) bidirectional strategy, (b) unidirectional strategy
<b>Fig. 4.30</b>	Linear fit plots for bidirectional strategy; (a) top, (middle) and (c) bottom

<b>Fig. 4.31</b>	Linear fit plots for unidirectional strategy; (a) top, (middle) and (c) bottom
<b>Fig. 4.32</b>	Schematic for TRR
<b>Fig. 4.33</b>	Reflected signal intensity measurement; (a) with filter, (b) without filter
<b>Fig. 4.34</b>	Discontinuity detection using TRR; graph for the respective bead is plotted against it, which shows the fluctuations whenever a discontinuity is occurring

## LIST OF TABLES

<b>Table 2.1</b>	Effect of LAM-DED process parameters on deposits
<b>Table 3.1</b>	Composition of In-617 powder used in LAM-DED
<b>Table 3.2</b>	Composition of In-617 wire used in WAAM
<b>Table 3.3</b>	Material challenges related to Inconel 617
<b>Table 3.4</b>	Overcoming the challenges using AM
<b>Table 4.1</b>	Single track deposition parameters
<b>Table 4.2</b>	Deposited tracks geometry at different parameters
<b>Table 4.3</b>	Tensile test results
<b>Table 4.4</b>	Deposition parameters for WAAM
<b>Table 4.5</b>	Taguchi's L-9 model
<b>Table 4.6</b>	Track geometry
<b>Table 4.7</b>	Tensile test results for bidirectional strategy
<b>Table 4.8</b>	Tensile test results for unidirectional strategy

## ACRONYMS

S. No.	Acronym	Expansion
1	AM	Additive Manufacturing
2	3D	Three Dimensional
3	DED	Directed Energy Deposition
4	LAM-DED	Laser Additive Manufacturing – Directed Energy Deposition
5	WAAM	Wire Arc Additive Manufacturing
6	In-617	Inconel 617
7	TRR	Time Resolved Reflectivity
8	FESEM	Field Emission Scanning Electron Microscopy
9	EDS	Energy Dispersive Spectroscopy
10	XRD	X - Ray Diffraction
11	HV	Hardness Value
12	W.F.R	Wire Feed Rate



# Chapter 1

---

## Introduction

### 1.1 Additive Manufacturing

According to ISO/ASTM 52900, Additive Manufacturing or 3D printing is defined as the process of joining materials to manufacture parts using 3D model data[1]. This process is usually done by opting a layer-by-layer methodology, as opposed to the subtractive manufacturing methodologies, offering advantages such as reduced material wastage, ability to create complex geometries, and shorter production cycles. With various benefits over conventional methodologies, Additive manufacturing (AM) technologies are rapidly advancing in a variety of industries, including aerospace, automotive, medical, architecture, arts and design, food, and construction[2]. This process provides more design freedom and complexity, reducing material wastage and allowing the use of a wide range of materials, including metals, composites, plastics, ceramics, and biomaterials[2]. AM processes offer good amount of savings in terms of expenditures as well as the material. It is also proved that AM can be a viable technique for many applications, particularly with product development[1].

#### 1.1.1 Classification of Additive Manufacturing

As per the ISO/ASTM 52900, AM processes can be broadly classified into seven different categories[1], as discussed below. Fig. 1.1 shows the classification of the different AM categories.

**(i) Vat photo – polymerization (VP):** This technique involves selectively curing a vat of liquid photopolymer resin with a light source (laser or projector) to form solid layers.

**(ii) Sheet lamination (SL):** This technique creates parts by stacking and bonding sheets of material, which are then cut into desired shape layer by layer.

**(iii) Material jetting (MJ):** This technique involves the deposition of build material droplets, which are then cured (typically by UV light).

**(iv) Powder Bed Fusion (PBF):** Powder bed fusion is the technique of selectively fusing regions of a powder bed using a laser or electron beam. A thin layer of powder is applied to the build platform, and energy selectively fuses it into a solid part.

**(v) Material Extrusion (ME):** This method involves pushing material (usually a thermoplastic filament) through a heated nozzle, where it melts and is deposited layer by layer.

**(vi) Directed Energy Deposition (DED):** DED uses focused thermal energy to melt material as it is deposited. Material is typically fed in the form of wire or powder.

**(vii) Binder Jetting (BJ):** In binder jetting, a liquid binding agent is selectively deposited to join powder particles. The process occurs in a powder bed, like PBF, but without melting the material.

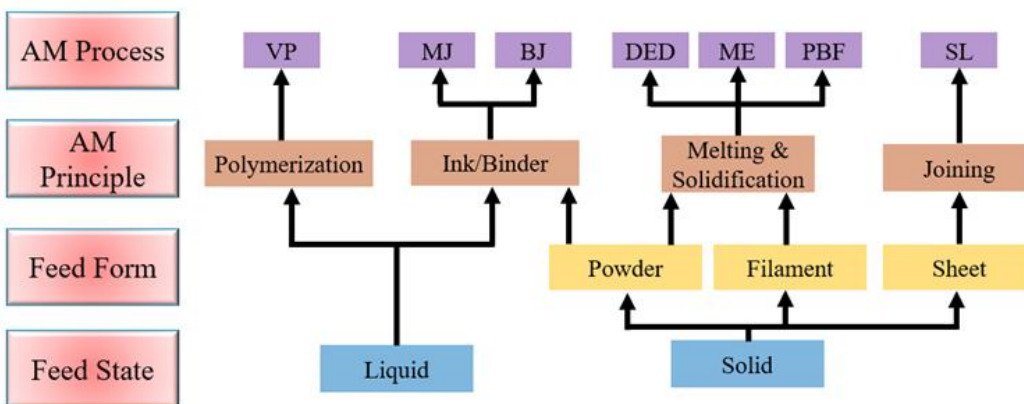


**Fig. 1.1: Types of Additive Manufacturing Processes.**

Among the various AM classifications discussed, metal additive manufacturing has drawn a lot of attention for its ability to produce high-performance components, particularly for aerospace, power generation, and tooling applications. Directed Energy Deposition (DED) processes are important in this domain because they can build near-net-shape parts, repair critical components, and process a variety of metallic alloys. Two of the most prominent DED – based techniques include:

- 1. Laser Additive Manufacturing – Directed Energy Deposition (LAM-DED)**, which utilizes a focused laser beam to melt the feedstock (powder or wire) as it is delivered to the substrate.
- 2. Wire Arc Additive Manufacturing (WAAM)**, which employs an electric arc as the heat source and uses wire as feedstock.

These processes are particularly well-suited for the additive manufacturing of high-temperature alloys such as Inconel 617, which are difficult to manufacture using traditional methods. The following sections delve deeper into these two techniques, describing their working principles, benefits, limitations, and suitability for fabricating complex metallic structures.

### **1.1.2 Laser Additive Manufacturing – Directed Energy Deposition (LAM-DED)**

Amongst numerous AM techniques, Laser Additive Manufacturing (LAM) stands out for its versatility and precision. It is a fabrication method for manufacturing engineering components from 3-D model data, using high-power lasers as an energy source to selectively melt or fuse materials (powder or wire form) to design distinct components[3]. In this, the laser beam creates a molten pool on the surface of a substrate while the metal feedstock - usually metallic powder delivered through a coaxial or lateral (off-axis) nozzle - is simultaneously fed into this melt pool. This process offers excellent control over thermal input, localized heating, and high deposition accuracy, making it highly suitable for high-performance materials such as nickel-based superalloys. The DED process can be classified into powder and wire feeding types according to the feedstock. Wire feeding DED processes produce significantly higher deposition rates and layer thicknesses compared to powder feeding processes[4]. LAM-DED has been successfully employed in the processing of wide range of metals and their alloys, among which Ni based superalloys find applications in various engineering sectors due to unique properties of these alloys such as oxidation and corrosion resistance, high temperature strength, etc[5]. There are two types of powder feeding methods, which are most used, i.e. off-axis feeding and coaxial feeding, which are being depicted in Fig. 1.2. The LAM-DED processes



have been extended to include repair, restoration, and remanufacturing, despite their primary use in the early stages of the fabrication of metallic parts with a near-net shape[4]. In summary, using LAM-DED for depositing Inconel 617 offers distinct advantages, such as ability to produce complex components with minimal material wastage and faster production times compared to conventional methods.

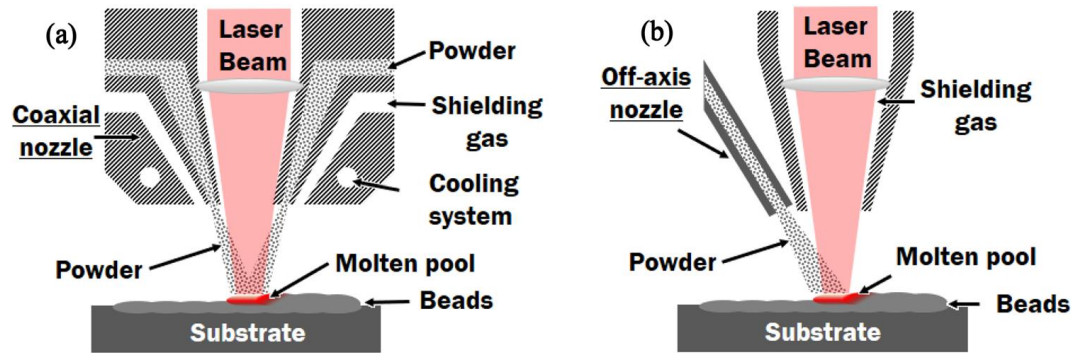


**Fig. 1.2: Powder feeding methods in LAM-DED, (a) Coaxial and (b) Off-axis[4]**

### 1.1.3 Wire Arc Additive Manufacturing (WAAM)

Wire arc additive manufacturing (WAAM) is an AM technology used in metal fabrication. Based on a 3D virtual model of the part, it utilises metallic wire as feedstock material and an electric arc to melt and deposit metal along a pre-programmed path[6]. It can easily generate large structural components (1000-3000 mm) with a high deposition rate (50-130 g/min), making it ideal for producing near-net-shaped elements[7]. WAAM has higher heat input and lower cooling rates than other metal additive manufacturing processes. This is useful for most commercially available materials[8]. It uses wire and electric arc to build components layer-by-layer, resulting in significant cost savings over powder and other fusion sources[9].

Different arc-based welding techniques are employed in WAAM, which are, **Gas Metal Arc Welding (GMAW/MIG)**, **Gas Tungsten Arc Welding (GTAW/TIG)** and **Plasma Arc Welding (PAW)**. Fig. 1.3 shows different WAAM techniques. GTAW-based WAAM uses a non-consumable tungsten electrode to generate heat and melt a filler wire to achieve the desired part geometry and PAW is a precision arc welding process that uses a constricted arc to generate a high-energy plasma jet for melting and depositing metal wire. In GMAW, electric arc is formed between a

metal workpiece and a consumable wire. This technique is highly implemented in large-scale part production due to its high deposition rate and energy efficiency. GMAW is further divided into Metal Inert Gas (MIG) and Metal Active Gas (MAG), each of which is suitable for a specific metal type, with MIG serving non-ferrous metals and MAG ideal for ferrous metals. GMAW has four metal transfer modes, each with its own unique welding current and electrode type. The Cold Metal Transfer (CMT) welding process marked a significant advancement in WAAM, as it reduced heat input and spatter levels. CMT, which is based on the short-circuit transfer mode, includes several modes each with its own set of characteristics.

Wire Arc Additive Manufacturing (WAAM) has emerged as a promising solution for fabricating large-scale metallic components with high deposition rates and material efficiency. Its ability to integrate multiple sensors and control systems makes it an ideal platform for developing and implementing in-situ monitoring techniques, which are critical for quality assurance and defect mitigation in real time.

WAAM has been chosen as the primary fabrication technique for this study over other AM methods such as LAM-DED due to its scalability, higher material efficiency, and process simplicity. The following chapters will go over the optimisation of WAAM parameters for Inconel 617 deposition, the development of multi-layer builds, and the introduction of a new in-situ monitoring approach called Time Resolved Reflectivity, which improves understanding and control of the WAAM process.

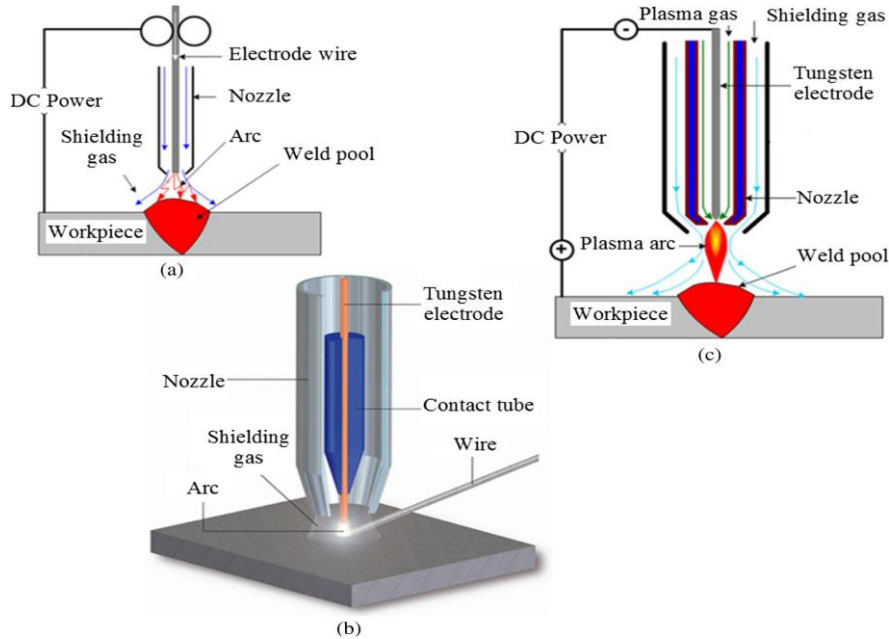


**Fig. 1.3: Different WAAM Techniques; (a) GMAW, (b) GTAW and (c) PAW[10]**

## 1.2 In - Situ Monitoring

Additive Manufacturing (AM) processes, such as Laser Additive Manufacturing-Directed Energy Deposition (LAM-DED) and Wire Arc Additive Manufacturing (WAAM), are inherently complex, requiring rapid, localised melting and solidification. This complexity frequently results in process instabilities and defects like porosity, lack of fusion, cracks, and residual stresses. To ensure the integrity and repeatability of AM components, in-situ monitoring has emerged as a critical aspect of modern AM systems. Real-time observation and measurement of critical process variables and material reactions during fabrication is known as **“in-situ monitoring”**. This allows for the early identification of irregularities and, in more sophisticated systems, closed-loop process control.

### 1.2.1 Various Monitoring Techniques in AM

Due to the dynamic and intricate nature of Additive Manufacturing (AM) processes, in-situ monitoring techniques must be utilised to ensure the structural integrity and consistent quality of fabricated components. Variations in melt pool behaviour,

material flow, and thermal gradients can result in flaws like distortion, porosity, delamination, or lack of fusion. A variety of monitoring methods, based on spectroscopic, thermal, optical, and acoustic principles, have been designed and incorporated into AM systems to address these issues[11]. By allowing for real-time observation and data collection throughout the build process, these methods offer insightful feedback that complements both closed-loop control strategies and open-loop diagnostics. Some of the commonly used systems are described below:

- (1) **Optical Monitoring:** High-speed visible and infrared (IR) cameras are frequently used to track layer geometry, observe wire feed or powder flow, and monitor the melt pool. Deviations in melt pool size, spatter, or layer uniformity - all of which are frequently signs of defects - can be found by examining photos and thermal maps[12].
- (2) **Pyrometry and Thermal Imaging:** Non-contact temperature readings of the melt pool and its surroundings are obtained using pyrometers and infrared cameras. Predicting the evolution of microstructures and comprehending solidification dynamics depend on precise thermal profiles. Under different emissivity conditions, accuracy can be increased by using multi-wavelength pyrometry.
- (3) **Machine Learning Algorithms:** Recent developments use machine learning algorithms to evaluate streams of data from multiple sensors, allowing for automated defect detection and process optimisation.
- (4) **Layer-wise Quality Assessment:** After every pass, some systems use layer-wise imaging and analysis to find contamination, surface irregularities, or incomplete fusion. This data can help guide post-processing choices or stop the process for remedial measures[13].
- (5) **Acoustic Emission (AE) Monitoring:** High-frequency elastic waves produced by material deformation or cracking during construction are detected by AE sensors. It is especially helpful in detecting the formation of defects.

**(6) X-ray or Synchrotron Imaging:** Advanced research methods for visualising internal features, such as porosity and keyhole dynamics, are still too complicated and expensive for industrial settings.

In this study, we have employed a novel technique of Time Resolved Reflectivity (TRR) for real time monitoring of the WAAM process to study the melt pool behaviour as well as discontinuity detection during the deposition. In the following section, we will discuss the underlying principle in more detail.

### **1.2.2 Time Resolved Reflectivity (TRR)**

Time-resolved reflectivity (TRR) is a technique for tracking how a sample's reflectivity changes over time, usually in response to an external stimulus such as a temperature change or a laser pulse. It relies on detecting changes in the intensity of reflected light from the surface of the material as a function of time. Basically, it is a sophisticated, in-situ optical diagnostic method that is frequently used to track surface melting, quick phase transitions, and other dynamic processes that occur during laser-material interactions, like those that occur in laser processing and additive manufacturing[14]. TRR relies on the fact that the reflectivity of a material changes when the thickness of a layer with a different refractive index (like the interface between amorphous and crystalline silicon) changes. These changes cause constructive and destructive interference, which can be measured by detecting the reflected light. The TRR setup that we designed to be used in the WAAM machine consists of a photodetector on one side of the WAAM torch and a handheld laser with a wavelength of 532 nm on the other. A filter was positioned in front of the photodetector to eliminate the errors caused by the WAAM spattering and ambient light. Designing and implementation of the TRR setup with WAAM will be discussed in detail in following chapters. Fig. 1.4 shows the schematic of the TRR setup.

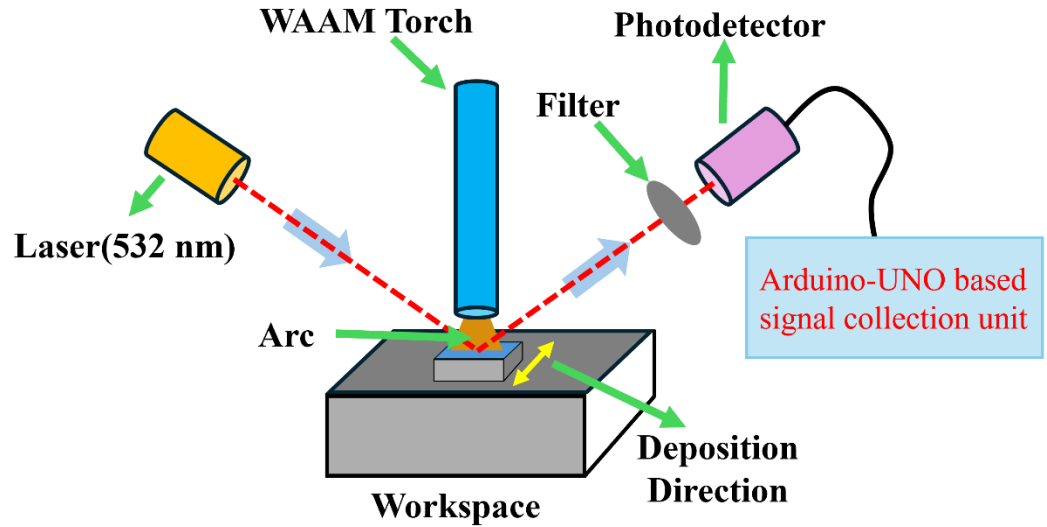


**Fig. 1.4: Schematic of TRR Setup**

### **1.3 Motivation of the present study**

The motivation for this research stems from the critical need for advanced materials and manufacturing strategies that can withstand the severe environmental conditions encountered in next-generation power plants. This section discusses both the application-driven rationale for choosing Inconel 617 and the technological impetus for using additive manufacturing methods like Laser Additive Manufacturing-Directed Energy Deposition (LAM-DED) and Wire Arc Additive Manufacturing (WAAM).

#### **1.3.1 High-Temperature Thermal Power Plants: The Need of the Day**

High-temperature thermal power plants have the potential to replace traditional coal-fired power plants by operating at supercritical and ultra-supercritical temperatures, resulting in improved energy efficiency as compared to traditional power plants. Thermal power plants should have high input temperatures and low rejection temperatures to achieve high efficiency. Modern research focusses on developing superalloys that can withstand high steam temperatures and pressures in energy systems and sub-systems[15], [16]. Since, the efficiency of the powerplant and the greenhouse gases emission hold a direct relation with the operating temperature of the powerplants, therefore high temperature powerplants are the

need of hour[17]. In advanced thermal power plants, the use of high temperatures and pressures enhances both the efficiency of energy conversion and CO<sub>2</sub> reduction[17]. Fig. 1.5 shows the CO<sub>2</sub> emission reduction pathways. A pictorial representation of the progress of different thermal powerplants with operating specifications is shown in fig. 1.6.

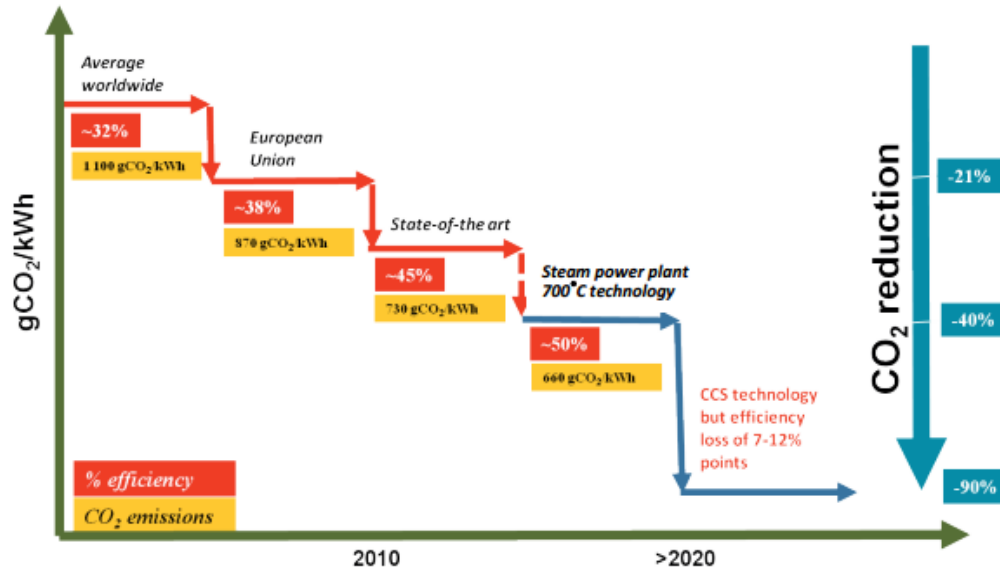


**Fig. 1.5: Indicative CO<sub>2</sub> emission reduction pathways** (Source: Adapted from VGB Power tech, 2012)

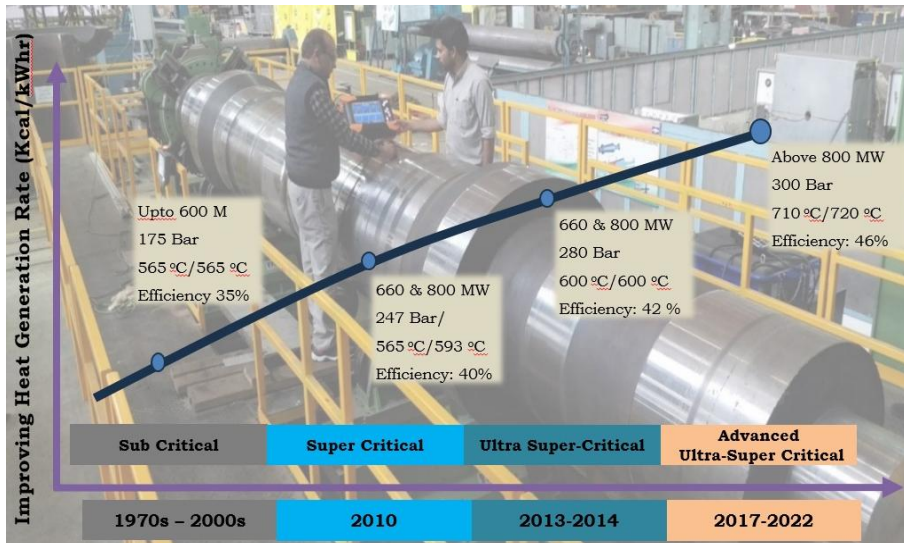


**Fig. 1.6: Progress of various thermal power plants** (Source: <https://heavyindustries.gov.in/advanced-ultra-supercritical-adv-usc-technology-thermal-power-plants>)

It is evident from Fig. 1.5 and Fig. 1.6 that with the increase in operating pressure and temperature, i.e. pressure of 300 bar and temperature more than 973 K (advanced ultra supercritical range), energy output as well as the conversion efficiency of the power plant increases, and the CO<sub>2</sub> reduces.

### **1.3.2 Alloy 617: The Backbone of Indian Advanced Ultra-Supercritical Thermal Power Plant Program**

Researchers in India and around the world face a significant technological challenge in this regard: choosing appropriate materials for high-temperature piping systems that have long-term microstructural stability, inherent resistance to mechanical deformation, and high-temperature corrosion resistance. It is necessary to investigate alternative high-temperature materials in this endeavour if the traditional ones, such as ferritic-martensitic steels (P91, P92), do not meet these standards. Utilising Ni-based superalloys is showing promise because of their superior oxidation, corrosion resistance, and creep rupture life, even at high pressures of 35 MPa and in the sophisticated ultra-supercritical conditions of 973 K to 1033 K (700 °C to 760 °C)[17]. One of the pioneers and top candidate piping materials for high-temperature applications among Ni-based superalloys is Alloy 617, which is anticipated to be employed in next-generation thermal power plants with operating temperature ranges of 973 K to 1033 K (700 °C to 760 °C) and pressures as high as 35 MPa. In actuality, the use of high-temperature ferritic steels is restricted to steam temperatures between 873 and 893 K (600 and 620 °C). Although the new alloys have been successfully developed for operating temperatures near ~ 923 K (650 °C), their vulnerability to oxidation on the steam side, where the temperature is extremely high, is the main intrinsic limiting factor in their use. Therefore, **Alloy 617**, Alloy 263, Alloy 740, and Alloy 800 are the candidate materials for the boiler components that are currently the subject of extensive investigation[17]. Alloy 617 exhibits excellent high-temperature stability. Under an oxidising atmosphere, Cr forms a dense oxide film of Cr<sub>2</sub>O<sub>3</sub>, which protects the alloy from environmental degradation by preventing inward diffusion of gases like oxygen and sulphur, as well as upward diffusion of metals. The combination of Al and Cr provides



additional protection against high-temperature oxidation, reducing oxidation and preventing corrosion at grain boundaries[18]. Boilers for advanced ultra-supercritical thermal power plants ( $> 973\text{ K}$ ) require the following essential parts: boiler tubes (hot sections), furnace walls, walls membrane, ultimate super-heater and re-heater stages and in- and outlet headers (extremely hot sections) as well as the thick-walled parts, particular the high-pressure outlet headers and the piping leading to the turbine[17]. Fig. 1.7 represents the outlet headers used in thermal powerplants.



**Fig. 1.7: Outlet header used in thermal power plants[18].**

Despite its superior material qualities, Inconel 617 presents considerable difficulties when manufactured with traditional methods like casting or machining. Because of the work-hardening nature of the alloy and its high melting point, these conventional methods frequently lead to significant material wastage, residual stresses, and challenges in creating complex geometries. Additionally, traditional fabrication methods take a long time and are expensive, especially when creating customised or low-volume parts for important uses. In this regard, Additive Manufacturing (AM) has become a game-changing strategy that overcomes a lot of these constraints. With AM, near-net-shape components can be fabricated layer by layer from a digital model, resulting in increased design freedom, lower lead times, and high material utilisation. High-performance alloys like Inconel 617 can be deposited using Directed Energy Deposition (DED) techniques like Wire Arc Additive Manufacturing (WAAM) and Laser Additive Manufacturing (LAM-DED). Large-scale parts with customised microstructures and regulated thermal profiles can be

produced using these methods. The initial motivation for investigating LAM-DED was its ability to regulate microstructural evolution in intricate geometries and its precise energy input. But the inherent drawbacks of LAM-DED, like its slower deposition rates, more complicated powder handling, and more expensive equipment, spurred a switch to WAAM. In contrast, WAAM provides better material efficiency because it uses wire feedstock, higher deposition rates, and is more cost-effective for large-scale industrial applications.

#### **1.4 Research Objectives**

The current study focuses on the **Realization of Inconel 617 in Additive manufacturing route for catering heavy industries, particularly the energy production sector**. This work aims to perform the parameter optimization of LAM-DED and WAAM and to investigate the mechanical properties of the additively manufactured Inconel 617 superalloy for the application in the High Temperature Powerplants. The primary objective of this research is to examine the viability, optimisation, and monitoring of Inconel 617 superalloy Additive Manufacturing (AM) using Wire Arc Additive Manufacturing (WAAM) and Laser Additive Manufacturing – Directed Energy Deposition (LAM-DED) techniques. Based on it, the study is structured around the following specific goals:

- (i) To conduct preliminary deposition and analysis using LAM-DED.
- (ii) To carry out the parametric optimization of the Wire Arc Additive Manufacturing of Inconel 617 based on Taguchi's L-9 model.
- (iii) To characterize the deposited Inconel 617 builds.
- (iv) To introduce and validate a novel in-situ monitoring approach using Time Resolved Reflectivity (TRR) in WAAM.

Fig. 1.8 depicts the plan of work.

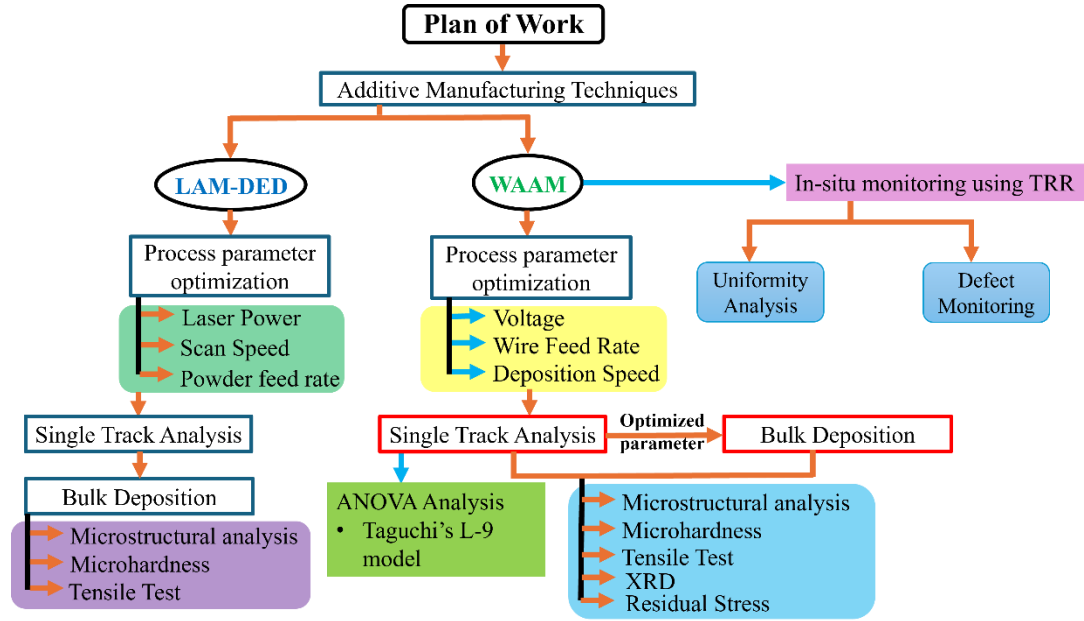


**Fig. 1.8: Plan of work**

## 1.5 Structure of the Thesis

There are five chapters in the thesis, a synopsis of which is provided below:

- **Chapter 1:** Introduces the additive manufacturing processes, in-situ monitoring, and motivation for the study.
- **Chapter 2:** Presents the literature review for the work explored in this thesis.
- **Chapter 3:** Provides the details of the material used, experimental setups and experimental procedures.
- **Chapter 4:** Presents the experimental investigations and their results.
- **Chapter 5:** Provides the conclusions obtained and the future directions for the work.

## Chapter 2

---

### Literature Survey

Additive Manufacturing (AM) is increasingly being used to manufacture components from advanced materials like nickel-based superalloys, particularly when complex geometries, tailored properties, and high-temperature performance are required. Inconel 617, known for its exceptional strength and oxidation resistance at high temperatures, is an excellent choice for critical applications in the power generation, aerospace, and nuclear industries[19]. However, conventional manufacturing of Inconel 617 presents significant challenges due to its low machinability, high tool wear, and difficulty shaping intricate geometries. To address these limitations, AM techniques - particularly Directed Energy Deposition (DED) using laser (LAM-DED) and arc-based Wire Arc Additive Manufacturing (WAAM) have been explored for fabricating In-617 components.

This chapter explores the current state of research on Inconel 617 additive manufacturing, focussing on both laser and arc-based methods, and highlights progress and gaps in the literature. It also discusses the various real-time in-situ monitoring techniques being developed and implemented in AM processes to improve consistency, detect defects, and ensure build quality.

#### **2.1 Current status on Additive Manufacturing of Inconel 617 superalloy**

Recent developments in additive manufacturing (AM) have opened new possibilities for fabricating In-617 with greater design flexibility and reduced material wastage. Among the AM techniques, Laser Directed Energy Deposition (LAM-DED), and Wire Arc Additive Manufacturing (WAAM) are particularly suitable for high-temperature alloys due to their ability to produce near-net-shape components with tailored microstructures[20], [21].

### 2.1.1 LAM-DED

Several studies have focused on LAM-DED of Inconel 617. Ahn et al.[22] reported that laser parameters significantly affect the melt pool dynamics and resulting microstructure, with finer grain structures forming at higher cooling rates. Zhang et al.[23] investigated the microstructural evolution in In-617 during laser deposition and observed significant columnar grain growth along the build direction, as well as interdendritic segregation of Mo and Cr. These chemical segregations were associated with microhardness variations and localized tensile weakness. Although laser-based systems offer high precision and good surface finish, limitations such as low deposition rates, high cost, and powder efficiency losses make them less attractive for large-volume production[24]. S. Yadav et al.[3] have performed parametric investigations on the track geometry of the copper-nickel graded layers (CuNi50) deposited on LAM-DED. Authors have employed ANOVA analysis to study the effect of laser power and scan speed on track geometry, i.e. track height and track width. Fig. 2.1 shows how the track dimensions are varying with laser power and scan speed.

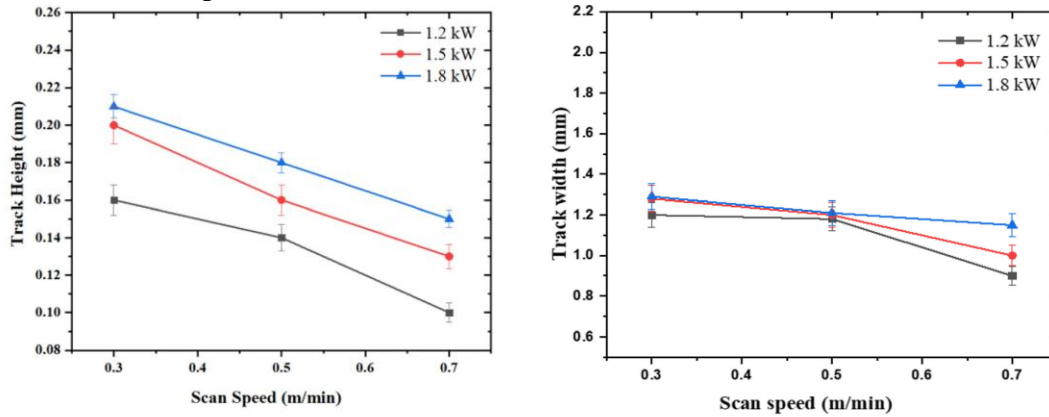


**Fig. 2.1: Effect of laser power and scan speed on track height(left) & track width(right)[3]**

Pal et al.[25] used LAM-DED for fabricating Inconel 617 thin-walled structures and reported columnar grain structures with micro segregation in the interdendritic regions. However, the process exhibited sensitivity to parameters such as laser power, scan speed, and powder feed rate, which directly affected the porosity and

microstructure. Jinoop A et al.[5] have discussed the Laser-assisted directed energy deposition of nickel super alloys in their review paper. Table 2.1 provides the details of various process parameters and their effect on the deposits in LAM-DED.

**Table 2.1: Effect of LAM-DED process parameters on deposits[5]**

S. No.	Process Parameter	Effect on increasing parameter
1.	Laser Power	Track Width and height increases. Better bonding with previous layers.
2.	Scan speed	Track Width and height decreases. Refined grains and enhanced strength.
3.	Powder feed rate	Increase in track height.
4.	Laser spot size	Increases minimum feature size.

### 2.1.2 WAAM

WAAM, in contrast to LAM-DED, utilizes wire feedstock and electric arc energy, offering higher deposition rates, lower feedstock cost, and excellent material utilization, which is critical for industrial-scale applications. Studies by Avinash B et al.[26] and Hassel T et al.[27] demonstrated successful deposition of Inconel-617 superalloy using WAAM with stable arc behavior and promising mechanical properties. However, challenges such as layer band formation and inter-dendritic segregations need further investigation. Avinash B et al. focused on the microstructure analysis and mechanical properties of Inconel-617 fabricated by WAAM. Microstructural analysis found cellular and equiaxed dendrites in the bottom layers but elongated columnar dendrites up to 2 mm in the middle and top layers due to varying cooling rates and temperature gradients and the microhardness varies between 257 HV and 274 HV[26]. Fig. 2.2 shows the microstructural analysis of WAAM deposited Inconel 617.

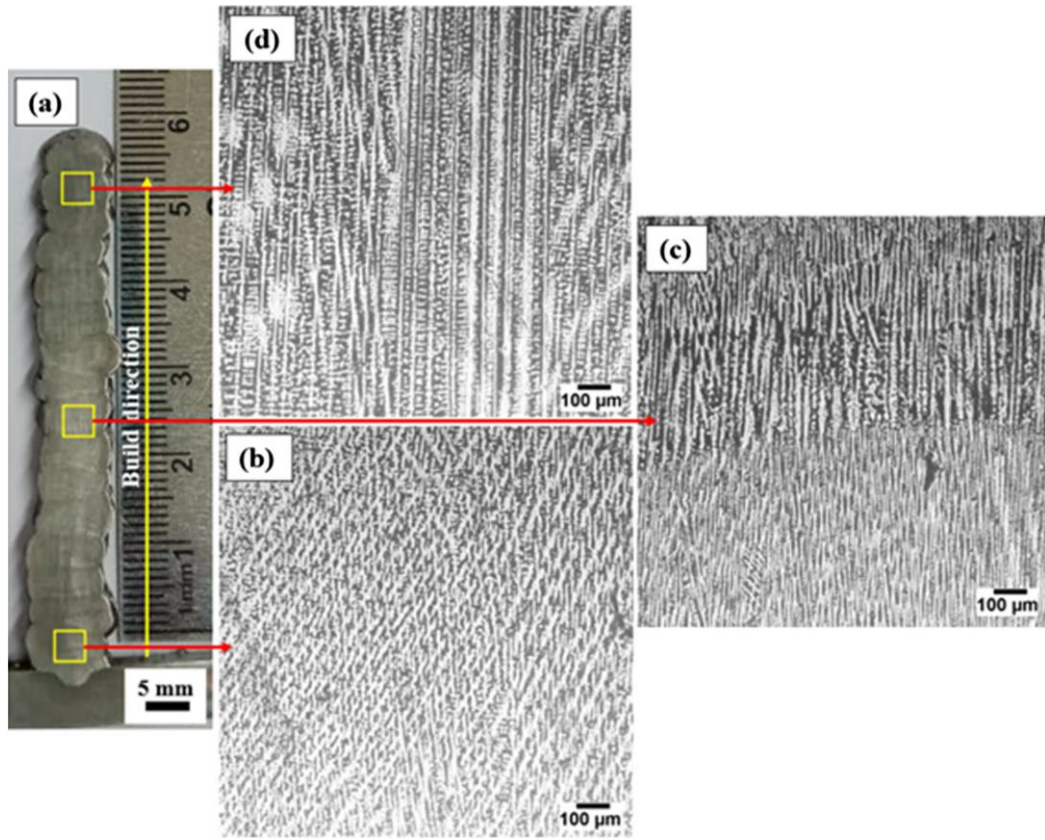


**Fig. 2.2: Optical micrographs of the as-deposited In-617 wall at different locations along the building direction[26]**

Hassel T et al.[27] investigated the anisotropy behavior of In-617, deposited by robotic WAAM. To analyze the grain growth, authors have used the diffraction images at different locations. They concluded that if the diffraction patterns are identical then the grain growth will be same over several layers or there will be two grains with nearly identical orientation. Fig. 2.3 shows the method employed for checking the grain growth. In another literature, Thayumanavan S et al.[28] have done the investigations on the MIG welding of In-617. Kumar G et al.[29] have employed various machine learning algorithms to predict the high temperature tensile strength of In-617 welded joints. They have used several ML approaches, which comprise of Linear regression, Decision tree regression, random forest regression, polynomial regression, gaussian process regression and support vector regression.

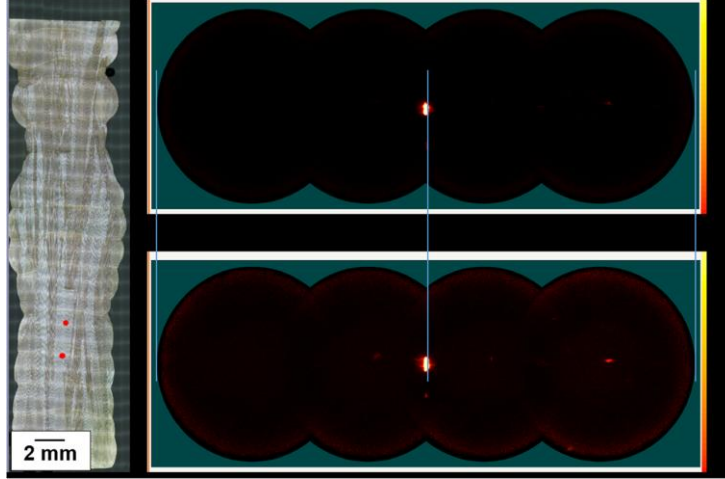


**Fig. 2.3: Analysis of grain growth[27]**

After applying various statistical approaches, it was observed that the Polynomial regression algorithm gives better response in case of the Statistical values of ultimate strength, elongation and yield strength[29]. Pramod Kumar G et al.[30] studied the microstructural and mechanical properties of In-617 joints welded by Laser-MIG hybrid welding. XRD analysis revealed the gamma and gamma prime phases along the presence of minor carbide peaks. Presence of Molybdenum in the weld metal caused the hot cracking in the fusion zone. The corrosion rate of the surface, evaluated using polarization curves analysis, slightly deteriorated from 0.342 to 0.427 mpy after hybrid laser MIG welding[30]. Since, the heat input in hybrid laser welding is from two sources, i.e. laser source and arc heat source. Both the heats were calculated by using the formulas mentioned below.

$Q_{\text{arc}} = 0.75 \times (A \times V \times 60) / (v \times 1000)$ , Here A = arc welding current, V = voltage and v = welding speed.

$Q_{\text{laser}} = 0.6 \times (W \times 60) / v$ , Here W = laser power and v = welding speed.

Total heat input was calculated by using the above-mentioned formulas.

## **2.2 Need for Real time monitoring in Additive Manufacturing**

Process monitoring in AM is essential to ensure consistency, detect anomalies, and improve quality control. Due to the layer-wise build nature of AM, each layer introduces the possibility of defects such as porosity, lack of fusion, thermal



distortion, or surface roughness. Real-time monitoring techniques aim to detect these issues during fabrication, allowing for corrective actions or feedback control[11]. Jeon et al.[31] have estimated the melt pool depth during the directed energy deposition by using a coaxial IR camera, laser line scanner and ANN. Authors have employed image processing to estimate the melt pool length and width, as shown in fig. 2.4 and integrated system is shown in fig. 2.5.

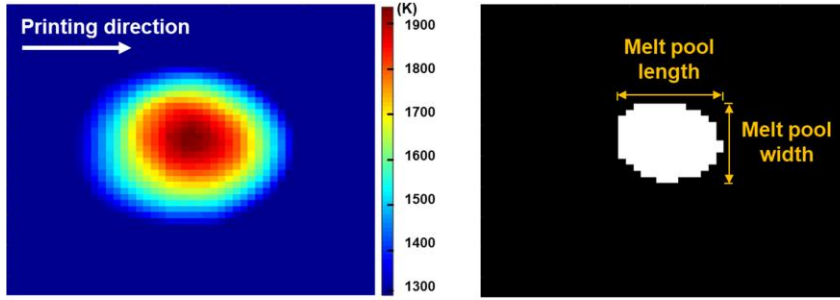


**Fig. 2.4: Real-time measurements of the melt pool width and length using coaxial IR camera[31]**

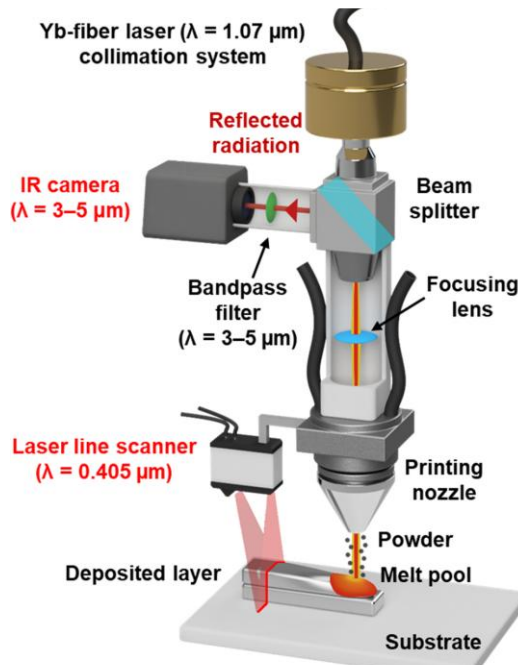


**Fig. 2.5: Melt pool depth estimation system for DED process[31]**

Miao L et al.[32] proposed a closed loop feedback control to maintain the stability of the melt pool during laser DED. Authors have used Linear Quadratic Regulator (LQR) control theory and a Particle Swarm Optimization (PSO) algorithm, as

shown in fig. 2.6. The system mainly focussed on reducing the reliance on manual experience. Thin-wall deposition samples with constant width and variable width were used to assess the controller's performance.

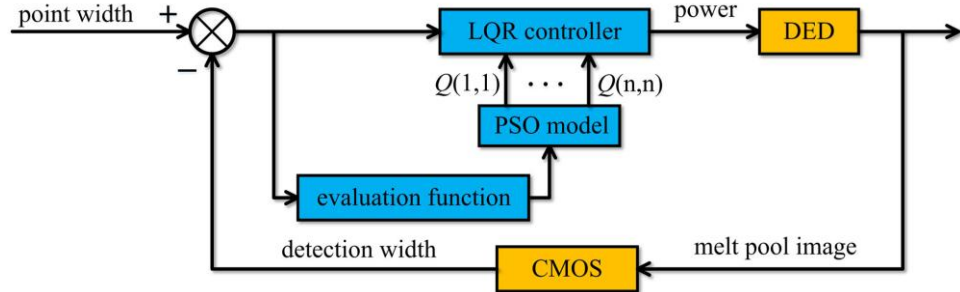


**Fig. 2.6: Structure diagram of LQR control system based on PSO[32]**

Smoqi Z et al.[33] have used a pyrometer based closed-loop control system to control the melt pool temperature and to mitigate flaw formation in laser-based DED. They have achieved a reduced variation in porosity and uniformity in microstructure in closed loop condition as compared to open loop condition. Akbari M et al.[34] developed an adaptable PI controller with layer-dependent control gains to maintain a stable melt pool width through the build. Image processing was implemented to obtain the melt pool width as shown in fig. 2.7. Thin wall sample deposition was used to assess the controller's performance. The results demonstrated that the controller could effectively maintain the melt pool width and generate a more homogeneous and finer microstructure by varying the laser power in real time.

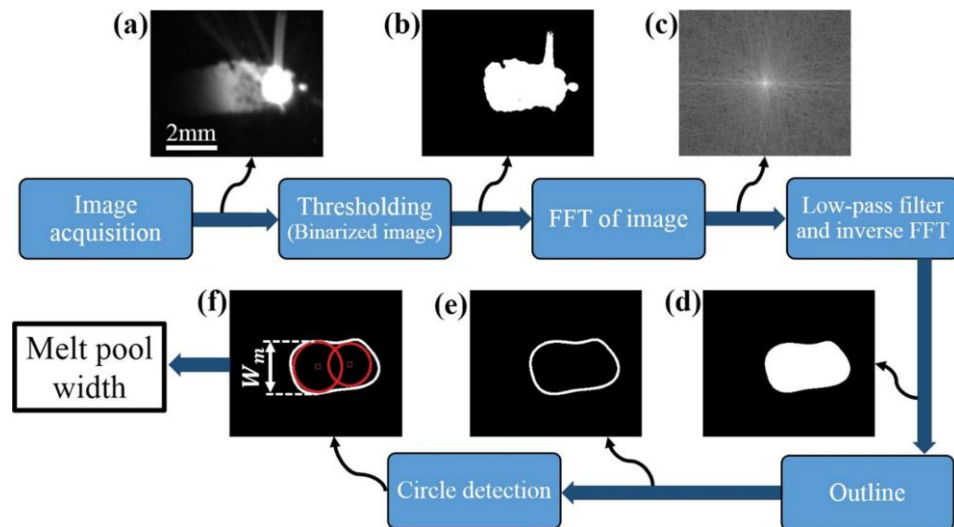


**Fig. 2.7: Image processing steps to obtain the melt pool width[34]**

Khan A et al.[35] worked on the in-situ temperature monitoring and feedback control in GTAW process. They have automated the GTAW process by replacing the foot pedal of GTAW power source with a control system, which consists of a DAQ and relay. Salehi D et al.[36] have implemented LabVIEW in laser blown powder cladding process to control the melt pool temperature. Feedback loop is shown below in fig. 2.8.

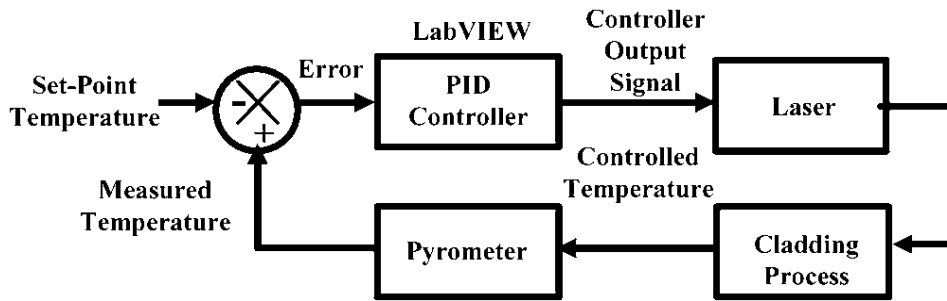


**Fig. 2.8: Temperature feedback loop[36]**

Myers A et al.[37] have employed a two-colour method to image the melt pool temperature and it can also be applied to any colour camera to monitor the melt pool.

This chapter has provided a thorough summary of the state of research on Inconel 617 additive manufacturing and real-time monitoring system integration, especially in relation to Directed Energy Deposition (DED) technologies. The second section reviewed several closed-loop control and in-situ monitoring techniques. The focus was on Laser DED, for which a sophisticated ecosystem of feedback systems and sensors has been created. However, monitoring in WAAM processes is still in its infancy, and there isn't much research on integrating feedback or real-time control. This shows a significant research gap and a creative opportunity. One significant step in overcoming these constraints is the use of cutting-edge methods such as Time Resolved Reflectivity (TRR) for WAAM, which is examined in this thesis.

## **Chapter 3**

---

### **Materials, Methods and Characterization Techniques**

This chapter provides a comprehensive overview of the materials, experimental setup, processing conditions, and characterization techniques used in this research. This research focusses on the additive manufacturing of Inconel 617 using two Directed Energy Deposition (DED) techniques: Laser Additive Manufacturing - Directed Energy Deposition (LAM-DED) and Wire Arc Additive Manufacturing (WAAM). While preliminary investigations were conducted using LAM-DED to better understand material compatibility and processing response, the primary body of work was completed using WAAM, beginning with the optimization of deposition parameters and progressing to bulk build-up and in-depth analysis. This chapter outlines the materials used, experimental setups for both LAM-DED and WAAM processes, and the optimization of process parameters. It also introduces a novel in-situ monitoring approach based on Time Resolved Reflectivity (TRR). Finally, the characterization techniques used to assess the microstructural and mechanical properties of the fabricated Inconel 617 samples are described.

#### **3.1 Material Specifications**

Nickel based superalloy, Inconel 617, also known by trade names Haynes 617 or Nicrofer 617 is a strengthened alloy and is recognized for its excellent combination of high temperature strength and resistance to oxidation[19]. This alloy was created in the 1970s and exhibits remarkable creep strength at temperatures higher than 950 °C in addition to good resistance to oxidation and corrosion[38]. It primarily consists of Nickel, Cobalt, Chromium, Molybdenum, with the addition of Aluminium enhancing its resistance to oxidation and carburization, especially at elevated temperatures. At elevated temperatures, alloy 617 shows very high levels of creep rupture strength, which makes it suitable for high-stress and long-term applications and is frequently utilized in the fabrication of important components

such as combustion cans, ducting and transition liners in turbines, as well as in heat-treating baskets and supports for catalyst-grids used in the production of nitric acid (HNO<sub>3</sub>)[19]. Apart from this, Inconel 617 alloy is a promising material for high temperature applications, including intermediate heat exchangers in gas-cooled reactors, re-heater components, and steam generator super heaters[39]. Table 3.1 and 3.2 displays the compositions of In-617 in powder and wire form respectively.

**Table 3.1: Composition of In-617 powder used in LAM-DED**

Cr	Co	Mo	Nb	W	Al	Ti	Fe	C	Zr	Ni
22	12.5	9	--	--	1	0.3	--	0.07	--	Bal.

**Table 3.2: Composition of In-617 wire used in WAAM**

Cr	Co	Mo	Nb	W	Al	Ti	Fe	C	Zr	Ni
21.68	12.86	9.25	--	--	1.13	0.48	2.5	0.07	--	51.62

### 3.2 Material challenges related to Inconel 617

Inconel 617, a solid-solution strengthened nickel-based superalloy, is well-known for its high-temperature strength, oxidation resistance, and structural stability, making it ideal for use in advanced power generation and aerospace systems. Despite its desirable properties, Inconel 617 poses several material-related challenges during manufacturing. These include poor machinability, rapid work hardening, segregations during thermal processing, etc. Table 3.3 provides a brief description of the material challenges related to In-617 and how can we overcome these challenges using AM as a solution is provided in table 3.4.

**Table 3.3: Material challenges related to Inconel 617**

<b>Machining Difficulties:</b>	High Tool Wear, Work Hardening
<b>Anisotropic Behavior:</b>	Due to the formation of directional grains during the machining/forming

<b>Porosity &amp; Inclusions:</b>	Common in casting process, due to gas entrapment or contamination
<b><math>\sigma</math>-Phase Precipitation:</b>	<ul style="list-style-type: none"> <li>▪ Topologically Close-packed (TCP) <math>\sigma</math>-Phase forms at higher temperatures.</li> <li>▪ Depletes Cr &amp; Mo from the matrix, resulting in reduced corrosion resistance.</li> <li>▪ Causes embrittlement.</li> </ul>

**Table 3.4: Overcoming the challenges using AM**

<b>Challenge</b>	<b>AM solution</b>	<b>Outcome</b>
<b>Tool Wear/costs</b>	Near-net-shape deposition	Reduces machining by 70–90%.
<b>Material wastage</b>	Powder/wire feedstock	Achieves 95% material utilization
<b>Anisotropic behaviour</b>	Isotropic deposition	< 5% property variation across axes.
<b><math>\sigma</math>-Phase Precipitation</b>	Layer wise microstructure control	Achieves $\gamma$ -matrix homogeneity with < 2% $\sigma$ -phase content.
<b>Porosity &amp; Inclusions</b>	Real-time monitoring	---

### 3.3 Experimental Setups

This section presents the experimental setups used for LAM-DED and WAAM processes, detailing the equipment, process parameters, and deposition strategies. It

also describes the integration of the Time Resolved Reflectivity (TRR) system for in-situ monitoring during WAAM.

### 3.3.1 Laser Additive Manufacturing - Directed Energy Deposition(LAM-DED)

An indigenously developed LAM-DED system at the Additive Manufacturing Technology Laboratory, RRCAT, is used in this study. Fig. 3.1 shows the pictorial view of the setup, while fig. 3.2 depicts the schematic of the LAM-DED.



**Fig. 3.1: 5-axis LAM-DED developed at RRCAT**

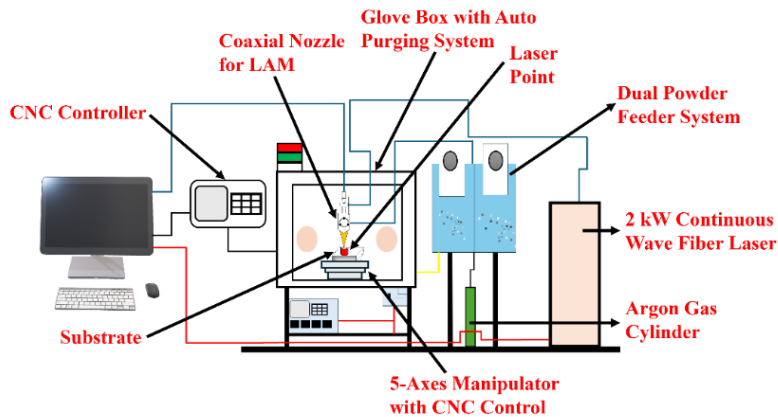


**Fig. 3.2: Schematic of the LAM-DED setup**

The deposition process was executed using a Continuous Wave (CW) fiber laser-based Directed Energy Deposition (DED) system with a maximum power of 2kW. This system uses high-power lasers as an energy source to selectively melt or fuse materials to design distinct components.

The system consists of several integrated subsystems, each of which plays an important role in the additive manufacturing process. The sub-systems are:

**(i) 5-axis Computer Numerical Control (CNC) manipulator in a controlled atmosphere chamber:** A 5-axis workstation is located within a controlled atmosphere chamber, also known as a glove box. Furthermore, the glove box includes a gas feeding mechanism designed to create an inert gas environment suitable for the LAM-DED process. The glove box design also includes an antechamber, which makes it easier to load and unload components onto the workstation while maintaining the controlled atmosphere. The parts which are to be built are first designed in MASTERCAM software.

**(ii) 2 kW Fiber Laser system:** The LAM-DED system includes a 2 kW Ytterbium doped fibre laser source (IPG Photonics, Model YLS-2000) with a nominal output power ranging from 50 W to 2050 W. The laser system operates at a wavelength of 1080 nm, with an output modulation rate of 50 kHz and a fast-switching time of 80  $\mu$ s.

**(iii) Powder feeder system:** The twin powder feeder system's primary function is to supply metallic powder to the nozzle. The system includes a motor and a rotating disc mechanism that delivers metallic powder within a size range of (45-106)  $\mu$ m at a set flow rate.

### **3.3.2 Wire Arc Additive Manufacturing (WAAM)**

Deposition of Inconel-617 is carried out on a gas metal arc welding (GMAW) based WAAM machine (**make; ESAB Inverter MIG 400**). The Repitier host device software uses G-codes to transmit the codes to the drivers, which in turn drive the DC motors for XYZ axis movement. In-617 wire with a diameter of 1.2 mm is continuously fed from a wire feeder to accomplish the intended function. In accordance with ISO 14175/I, a 99.9% argon gas was utilised as a shielding gas for WAAM deposited samples. The substrate was an identically sized SS-316 plate measuring 10 cm x 10 cm x 1 cm. To optimize the process parameters, pilot



experiments were carried out. Figs. 3.3 and 3.4 respectively represent the pictorial and schematic view of WAAM setup used for the experiments.

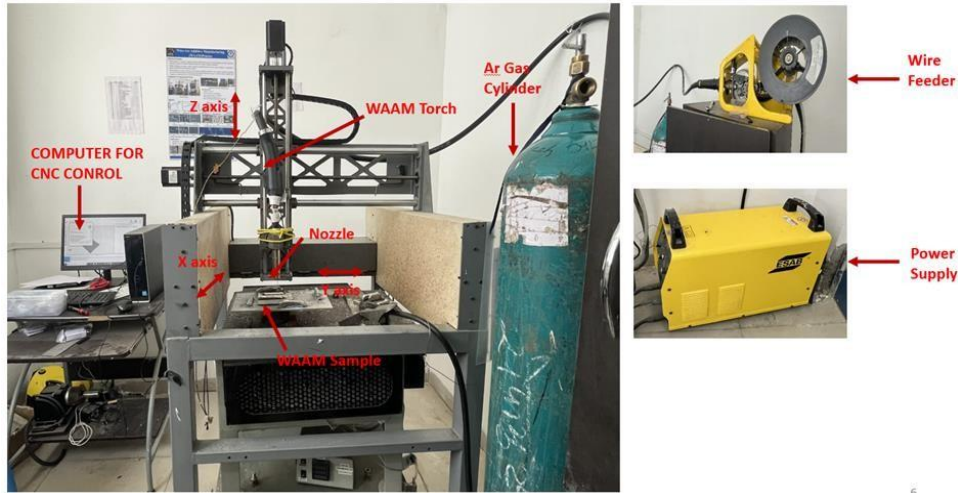


**Fig. 3.3: Pictorial view of WAAM setup**

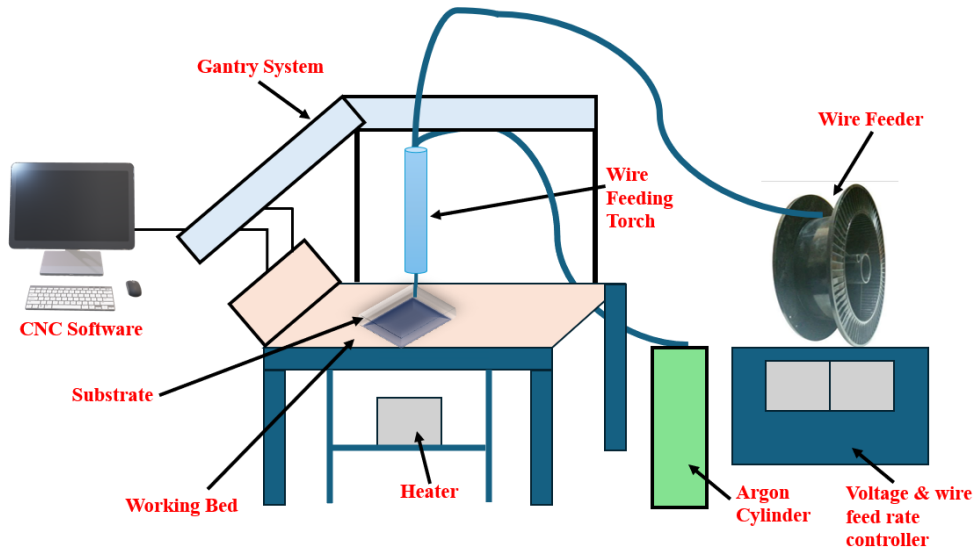


**Fig. 3.4: Schematic of the WAAM setup**

### 3.3.3 Time Resolved Reflectivity (TRR)

To ensure the integrity and repeatability of AM components, in-situ monitoring has emerged as a critical aspect of modern AM systems. In this study, we have employed a novel technique of Time Resolved Reflectivity (TRR) for real time monitoring of the WAAM process to study the melt pool behaviour as well as discontinuity detection during the deposition. A fixture as shown in fig. 3.5 is designed and integrated with the WAAM setup. To detect the reflective intensity signal, a photodetector was used and an Arduino-UNO based setup was employed

for data collection. Figs. 3.6 and 3.7 represents the schematic and the integrated TRR setup used in WAAM respectively.

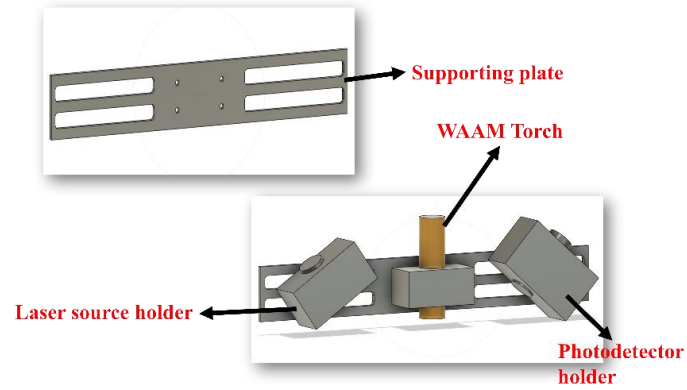


**Fig. 3.5: 2-D drawing of TRR setup**

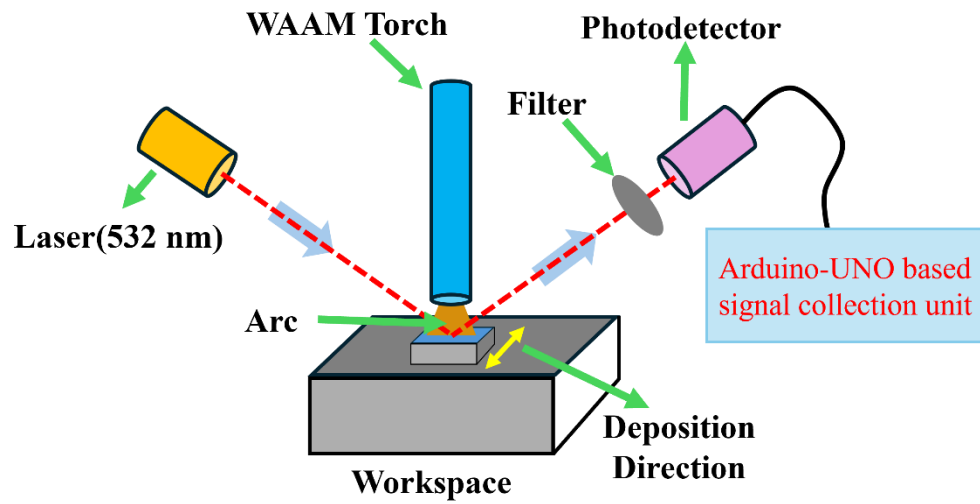


**Fig. 3.6: Schematic of TRR Setup**

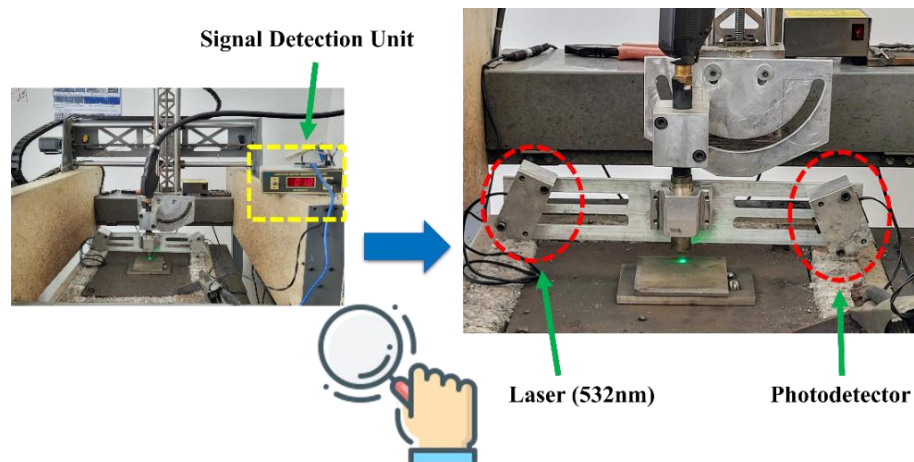


**Fig. 3.7: TRR setup implemented on WAAM**

### 3.4 Material Characterization

Material characterization was carried out to evaluate the microstructural features and mechanical properties of the Inconel 617 samples fabricated using LAM-DED and WAAM. Techniques such as optical microscopy, scanning electron microscopy (SEM), and microhardness testing were employed to analyze grain structure, defect formation, and hardness distribution across the deposited regions. These analyses helped in understanding the influence of process parameters and monitoring techniques on the final build quality.

#### 3.4.1 Metallographic Characterization

The samples deposited on LAM-DED and WAAM were cut using a wire EDM machine and were polished on a polishing machine, (**make; Chennai METCO**) in multiple steps to achieve a consistent, mirror-like surface finish. To begin, 80 grit paper was used to remove any surface irregularities. The surface texture was then further enhanced by using the finer grit sheets for further polishing, i.e. 220, 400, 600, 800, 1200, 1500, 2000 grit papers. After polishing, samples were carefully cleaned with acetone and ultrasonic cleaning was done to remove any external material. Microstructures of the sample were revealed by electrolytic etching at 5 V for 10-60 seconds using 10% oxalic acid solution as etchant and an inverted microscope was employed to capture the microstructural images.



**Fig. 3.8: Polishing Machine**

### 3.4.2 Field Emission Scanning Electron Microscopy (FESEM)

A Field Emission Scanning Electron Microscopy (FESEM) (**make; JEOL JSM-7400F**) was used to examine the elemental compositions and morphological analysis of the deposited samples. It is a high-resolution technique in which an electron beam emitted by a field emission source hits the surface of the sample beneath it. It is then raster scanned to determine the microstructure and surface morphology at various magnifications. For ideal imaging conditions, samples were firmly adhered to SEM stubs using conductive adhesive. The inner arrangement of the setup is such that the ejected electron beam passes through an arrangement of magnetic lenses and metal apertures in a vacuum tube before focussing as a thin monochromatic beam. When an incident electron beam interacts with a sample, it produces output beams in the form of backscattered electrons, secondary electrons, Auger electrons, and characteristic X-rays. Different detectors collect each type of electron, resulting in images of the sample specimen. To determine the elemental composition, EDS analysis was performed. Studies were done using line scan or area scan, whichever required.



**Fig. 3.9: Field Emission Scanning Electron Microscopy (FESEM)**

### 3.4.3 Energy Dispersive Spectroscopy (EDS)

Energy Dispersive Spectroscopy (EDS) is an analytical technique used in conjunction with scanning electron microscopy (SEM) to determine the elemental composition of a material. When high-energy electrons displace inner-shell electrons, the resulting electron transitions emit x-rays with energies unique to the elements present. An energy-dispersive detector captures the emitted x-rays and records their energies. The resulting energy spectrum reflects the sample's elemental composition. Spectral analysis identifies the elements in a sample by correlating peaks in the spectrum with known elemental standards. EDS is extremely useful in materials science, geology, forensics, and biology because it provides microscopic insights into a sample's chemical makeup, distribution, and morphology. Its non-destructive nature and high sensitivity make it an adaptable tool for a wide range of applications, including identifying trace elements in geological samples and characterising the elemental composition of biological tissues. In this study, compositional analysis of deposited samples was carried out using Energy Dispersive Spectroscopy (EDS) which was coupled with FESEM shown in fig. 3.9.



**Fig. 3.10: X-ray diffractometer using Cu-K $\alpha$  radiations**



### 3.4.4 X - Ray Diffraction (XRD)

Residual Stresses, crystal structure and phase transitions of the deposited samples were analysed using a Bruker D2 phaser X-Ray diffractometer using Cu-K $\alpha$  radiations with a wavelength of 1.5406 Å. Normal XRD scans were done throughout a  $2\theta$  range of  $10^\circ$  to  $90^\circ$ . The diffraction peaks were useful for determining phase compositions and crystalline structures. XRD basically works on the principle that when a high-energy beam strikes a target material, energy is absorbed and electrons jump from the inner to outer shell, resulting in an unstable state condition. Because electrons have a natural tendency to return to their initial stable state, they do so, emitting X-rays. Electrons moving from M to K shells produce K $\beta$  x-rays, while those moving from L to K shells produce K $\alpha$  x-rays. The basic principle of XRD analysis is based on Bragg's law, which states that "When a collimated beam of x-rays strikes a crystal, the atoms act as diffraction centres, and the diffracted beams combine to give diffraction patterns." For  $n^{\text{th}}$  order diffraction, using the X-rays of wavelength  $\lambda$ , the Bragg's equation is  $n\lambda = 2d \sin \theta$ . For residual stress analysis, an XRD scan at  $74.83^\circ$  (220 peak) for seven different tilt angles ( $\psi$ ) is performed and residual stress value was calculated using **d-spacing vs  $\sin^2\psi$**  method.

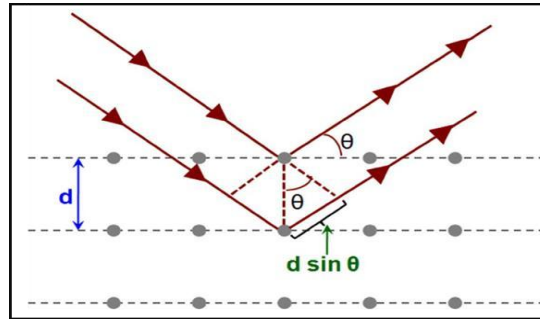


Fig. 3.11: Bragg's Law in a 2-D crystal

## 3.5 Mechanical Testing

### 3.5.1 Micro-Hardness Test

Vickers microhardness method was employed in the testing because of its precision in measuring minute variations in hardness across different microstructural regions. Vickers hardness setup (**make; METCO-Economet VH-IMDX**) was employed in the testing. Indentations were made with a 0.2 kgf (1.96 N) load with a dwell time of 10 seconds. To reduce the inaccuracies and to eradicate the errors, indentations

were taken at different locations. Hardness value was calculated by using the following formula:

**$HV = 1.854(P/D^2)$** , Here, P = load, D = (diagonal 1 x diagonal 2)



**Fig. 3.12: Vickers microhardness test setup**

### 3.5.2 Tensile Test

The tensile test was performed to assess the mechanical properties of the deposited material under uniaxial stress, revealing important information about its ductility and strength. A universal testing machine (*make, SHIMADZU*) (max. load 100 kN) was employed in conducting the tensile testing.

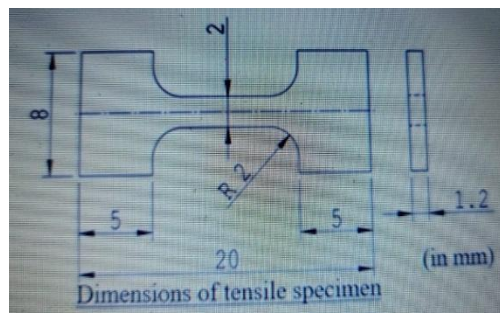


**Fig. 3.13: Universal testing machine (left) and 2-D drawing for micro- tensile sample(right)**

## **Chapter 4**

---

### **Experimental Investigations on Additive Manufacturing of Inconel 617 Superalloy**

This chapter describes the detailed experimental investigations performed to fabricate Inconel 617 using Laser Additive Manufacturing-Directed Energy Deposition (LAM-DED) and Wire Arc Additive Manufacturing (WAAM). The emphasis is on the process development, parameter optimisation, and performance evaluation of the fabricated samples. Initial trials were carried out using LAM-DED to better understand the alloy's behaviour during laser-based deposition, followed by a thorough investigation using WAAM due to its higher deposition rates and cost-effectiveness. Furthermore, a novel in-situ monitoring approach based on Time Resolved Reflectivity (TRR) was implemented in WAAM to observe and evaluate process stability in real time. The findings are evaluated in terms of deposition quality, geometrical stability, microstructure evolution, and mechanical performance.

#### **4.1 Preliminary experiments using LAM-DED**

Laser metal deposition is a complex process that involves intricate parameter interactions, intrinsic heat treatments, and metallurgical transformations. Understanding these dependencies is critical for successfully optimising the process. Because of absorptivity variations, each material responds differently to laser energy. As a result, it is critical to identify the optimal laser energy range for a given material. However, laser energy is only one of several variables involved in the process. Exploring the individual and interactive effects of different parameters is critical for achieving the desired results. Optimising process parameters entails



determining the optimal balance at which all parameters converge to produce maximum efficiency. This optimisation process is critical and difficult, necessitating meticulous analysis and experimentation to yield the desired results. Various pilot experiments were carried out for single track deposition. SS 316 plate was used as a substrate. The deposited tracks were visually and microscopically inspected for:

- (i) Uniformity in the deposition
- (ii) Stability of track dimensions
- (iii) Defects inclusions

#### **4.1.1 Single Track Analysis**

The experimental procedure was divided into two distinct stages. In the initial stage, single tracks of length 20 mm each were deposited. During this, critical process parameters such as laser power and scan speed were systematically varied while maintaining a constant powder feed rate. These parameters were carefully chosen to achieve defect-free deposition, focusing on producing an aspect ratio (height to width ratio) greater than 5[3], as summarized in Table 4.1. The track height and width for each deposit were measured using dial gauge and optical microscope respectively, and the corresponding aspect ratios were calculated, as shown in Table 4.2. Fig. 4.1 and fig. 4.2 shows the pilot experiments done for track deposition and the single-track deposition at the set parameters.

**Table 4.1: Single track deposition parameters.**

Parameters	Unit	Values
Laser Power(P)	Watts	600,650
Scan Speed(v)	mm/min.	600,700,800
Powder Feed Rate	gm/min.	5

**Table 4.2: Deposited tracks geometry at different parameters.**

S. No.	Laser Power	Scan Speed	Powder feed rate	Track Height(mm)	Track Width(mm)	Aspect Ratio
1	600	600	5	1.50	0.25	5.90
2	600	700	5	1.49	0.21	7.06
3	600	800	5	1.43	0.19	7.55
4	650	600	5	1.62	0.27	5.88
5	650	700	5	1.53	0.20	7.47
6	650	800	5	1.38	0.58	2.37

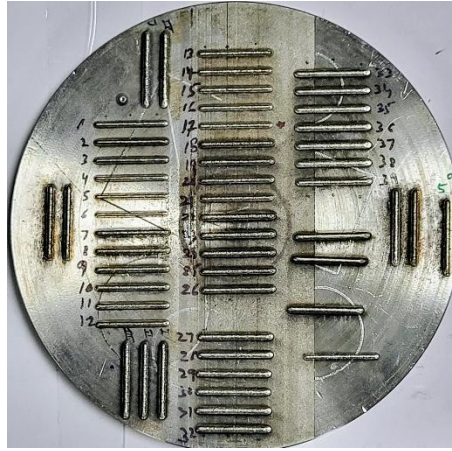


**Fig. 4.1: Pilot experiments done for parameter optimization**

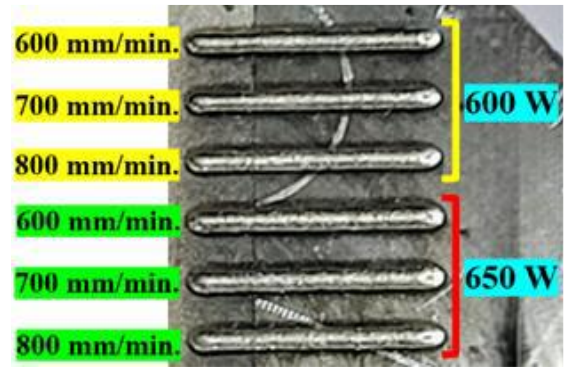


**Fig. 4.2: Single track deposition at optimized parameters**

#### 4.1.2 Bulk deposition

In the subsequent stage of the experimental procedure, bulk deposition was carried out to fabricate a block with dimensions of 50 mm × 50 mm × 6 mm, (depicted in fig. 4.3) using a layer-by-layer approach. The process parameters identified during the single-track deposition phase were employed to ensure consistent and defect-free bulk deposition. The deposited block was then subjected to further characterization to evaluate its microstructural and mechanical properties.

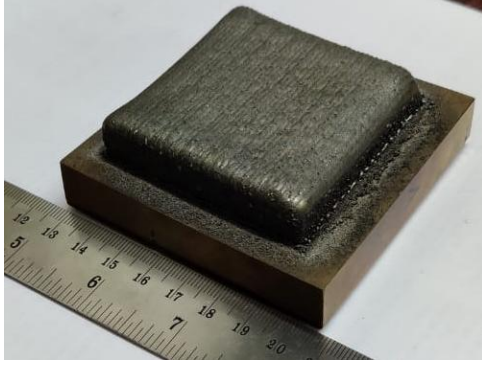


**Fig. 4.3: Deposited block using LAM-DED**

#### **4.1.3 Microstructural Analysis**

Microstructural analysis of the deposited Inconel 617 was conducted to assess the influence of the LAM-DED on its microstructural morphology. A specimen with dimensions 12 mm x 6 mm was cut out from the cross section of the block in the direction of the deposition using a Wire EDM machine and was mechanically polished. Microstructures of the sample were revealed by electrolytic etching at 5 V for 10- 60 seconds using 10% oxalic acid solution as etchant.

A rapid cooling rate is noticed at the bottom layers as compared to upper layers because the heat generated gets dissipated through the substrate during the deposition of initial layers[26] while in upper layers, heat dissipation don't take place easily, thus resulting in slower cooling rates and remelting of the deposited layers as well, resulting in the formation of fine cellular and equiaxed grains in bottom(initial) layers and columnar grains in the upper layers, as shown in fig. 4.4(a) & 4.4(b) respectively. Grain sizes across different layers are measured using line-intercept method. Across the bottom layers, grain size number(G) was 11.805 and average grain diameter was found to be 770.817 $\mu\text{m}$ . In the upper layers, grain size number(G) was 10.739 and average grain diameter was found to be 1143.285 $\mu\text{m}$ . During the deposition, the layer which gets deposited first doesn't get much time to solidify, and the successive layer gets deposited over it, causing the previously deposited layer to melt partially, which results in the formation of an interface between two successive layers, known as layer band formation[26], visible in fig. 4.4(c). Apart from this, inter-dendritic segregations(precipitates), which are also

susceptible to cracks were also observed along the grain boundaries, as shown in fig. 4.4(d).

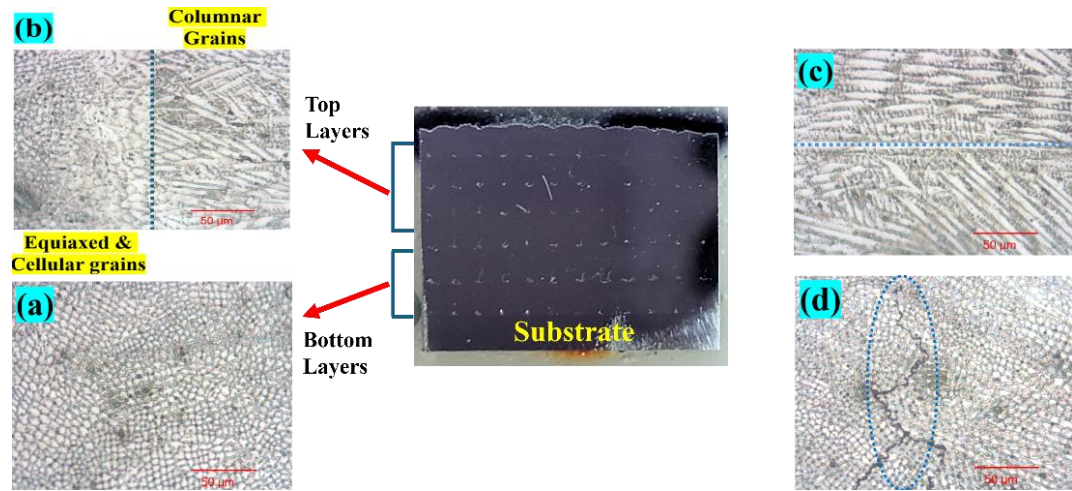


**Fig. 4.4: (a)Formation of cellular and equiaxed grains in bottom layer;(b) Initialization of columnar grains in the upper layers;(c) Layer band formation;(d) Inter-dendritic segregations**

#### 4.1.4 Microhardness Test

Vickers microhardness method was employed in the testing because of its precision in measuring minute variations in hardness across different microstructural regions. Indentations were made with a 0.2 kgf or 1.96 N load. The dwell time was 10 seconds. Five indentations were taken on each layer to find average hardness value, as shown in fig. 4.5(a). Microhardness values (HV) for each layer varied as:  $268.10 \pm 7.16$  (layer-1),  $252.52 \pm 4.90$  (layer-2),  $247.46 \pm 10.24$  (layer-3),  $244.18 \pm 2.40$  (layer-4),  $247.42 \pm 6.26$  (layer-5) and  $239.86 \pm 11.75$  (layer-6) respectively. It was observed that the lower layers exhibit higher hardness, which can be attributed to the presence of fine equiaxed and cellular grains. In contrast, the upper layers show reduced hardness, because they consist of coarse columnar grains, formed due to a slower cooling rate as compared to the bottom layers. Fig. 4.5(b) represents the

microhardness variation across the layers. grains, formed due to a slower cooling rate as compared to the bottom layers.

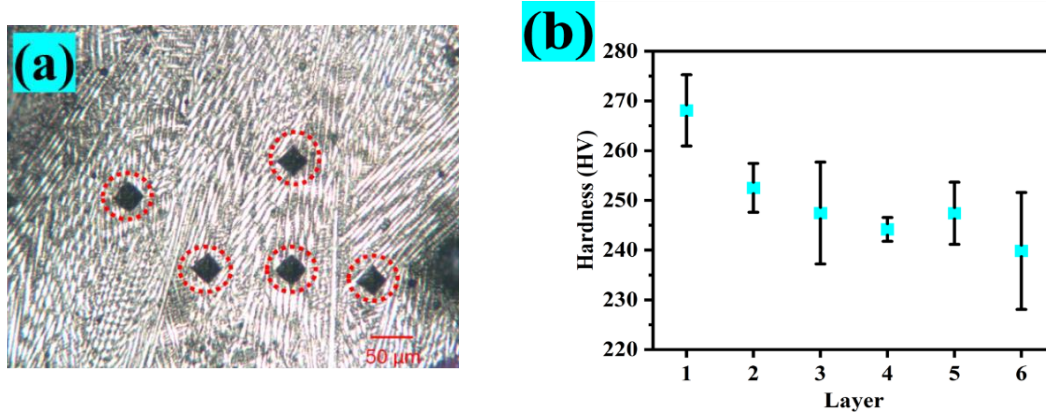


**Fig. 4.5: (a) Indentations on a single layer; (b) Microhardness value variations at different layers**

#### 4.1.5 Tensile Properties

The tensile test was conducted to evaluate the mechanical properties of the deposited material under uniaxial stress, which provides essential information about its ductility & strength. Dog-bone specimens with dimensions as shown in fig.4.6(a) were prepared for the test. The specimens were tested at a constant strain rate of 10mm/min using a universal testing machine to determine the yield stress, ultimate tensile strength, and elongation at break. Tests were performed for 3 specimens to evaluate the average values. Table 4.3 compiles the tensile test results and fig. 4.6(b) shows the stress-strain curve for all three specimens. The average tensile strength, elongation and yield stress were  $381.78 \pm 42.59$  MPa,  $31.3 \pm 6.934\%$  and  $202 \pm 95$  MPa respectively. According to ASTM B168-19, the average tensile properties of Inconel 617 are Ultimate Tensile Strength=655 MPa, Elongation=35% and Yield Stress=240 MPa[26]. The average elongation and yield stress of the samples are consistent with the ASTM B168-19 standards. However, the ultimate tensile strength is notably lower than the standard value, which can be due to the presence of interdendritic segregations, also susceptible to cracks. Segregations can lead to

variations in local chemical composition of the deposition, resulting in areas with differing mechanical properties, leading to brittleness and reducing the strength.

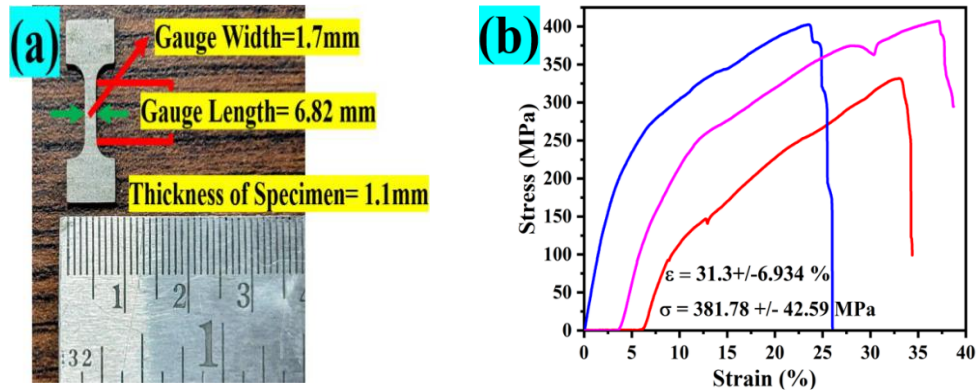


**Fig. 4.6: (a)Tensile test specimen;(b) Stress-Strain curve for the specimens.**

**Table 4.3: Tensile test results.**

	Max. Force( N)	Max. Displacement (mm)	Tensile Strength (MPa)	Yield Stress (MPa)	Elonga tion (%)
Sample 1	620.20	2.34	331.65	252	34.38
Sample 2	752.80	1.77	402.56	247	26.02
Sample 3	761.40	2.63	407.16	107	38.69

## 4.2 WAAM Analysis

Following the preliminary investigations with LAM-DED, extensive experimental studies were conducted using Wire Arc Additive Manufacturing (WAAM) to fabricate Inconel 617. The analysis began with the optimization of key process parameters through single-track depositions, followed by multi-layer and bulk builds. The resulting deposits were evaluated for their geometrical consistency, surface quality, and build integrity. WAAM demonstrated high deposition efficiency and cost-effectiveness, making it suitable for fabricating larger components. Detailed characterization was carried out to assess the microstructural features, including grain morphology and defect distribution, and to correlate them with the optimized parameters.



#### 4.2.1 Pilot experiments to optimize the process parameters

Pilot experiments were carried out to determine the significance of the WAAM process parameters on the quality of the produced part. The process parameters for the design of experiments model were chosen based on the pilot experiments for the parametric optimisation of the WAAM deposited part. Single tracks, as shown in fig. 4.7 were deposited by varying the process parameters, i.e. voltage, wire feed rate and deposition speed at various levels. Based on the uniformity of the deposition and consistency of track geometry, parameters were chosen for further deposition.



**Fig. 4.7: Pilot experiments for optimizing the process parameters of WAAM**

#### 4.2.2 Deposition Parameters for WAAM

After performing various pilot experiments for bead deposition, deposition parameters were finalised and were taken into consideration for further deposition. Table 4.4 depicts the deposition parameters for WAAM.

**Table 4.4: Deposition parameters for WAAM**

Parameters	Range	Unit
Voltage	15,16,17	Volts
Wire feed rate	3.5,4.5,5	m/min.
Deposition/Travel speed	150,200,250	mm/min.

#### 4.2.3 Development of Taguchi's L-9 model for WAAM deposition

Based on the above stated parameters, Taguchi's L-9 model, as depicted in Table 4.5 was developed with 3 factors, having 3 levels each.

**Table 4.5: Taguchi's L-9 model**

	Voltage(V)	Wire feed rate(mm/min.)	Deposition Speed(m/min.)
Parameter 1	15	3.5	150
Parameter 2	15	4.5	200
Parameter 3	15	5	250
Parameter 4	16	3.5	200
Parameter 5	16	4.5	250
Parameter 6	16	5	150
Parameter 7	17	3.5	250
Parameter 8	17	4.5	150
Parameter 9	17	5	200

#### 4.3 Single Track Analysis

Single tracks of 70 mm each were deposited at 9 different parameters, with three repetitions of each, as shown in fig. 4.9 and Anova analysis was used to generate the main effect plots. After the successful deposition of the single tracks at the specified parameters, track dimensions, i.e. track height and track width were calculated using dial gauge and optical microscope. Measurements were done according to the schematic as shown in fig. 4.8 and fig. 4.10 shows the optical microscope images of single tracks.

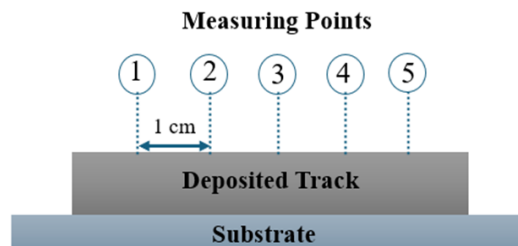


**Fig. 4.8: Schematic for the track geometry analysis**



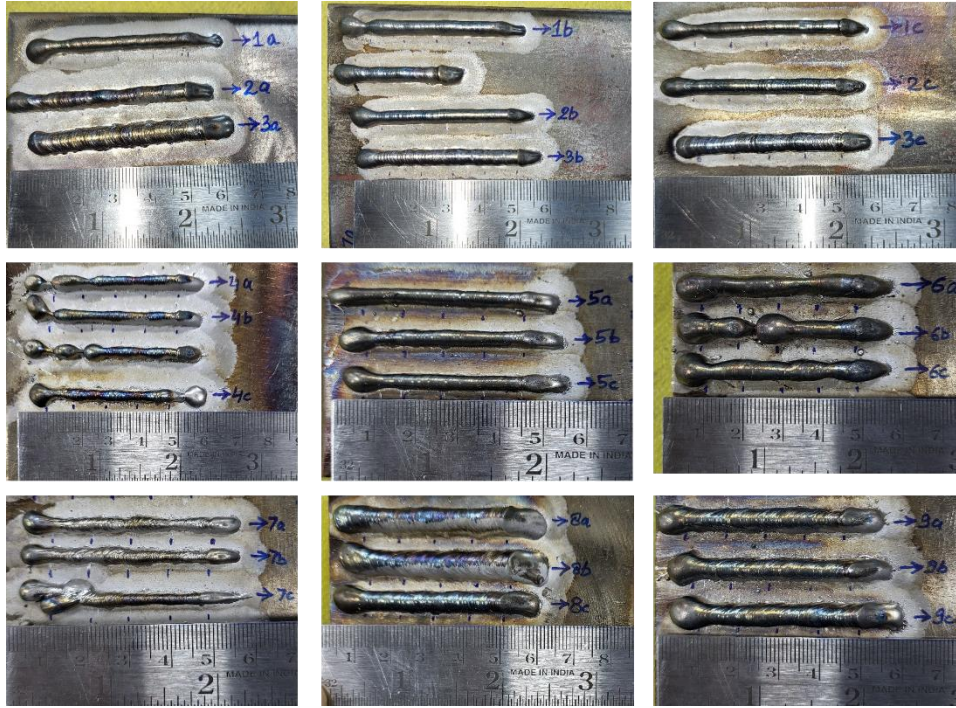


**Fig. 4.9: Single track deposition at various parameters**

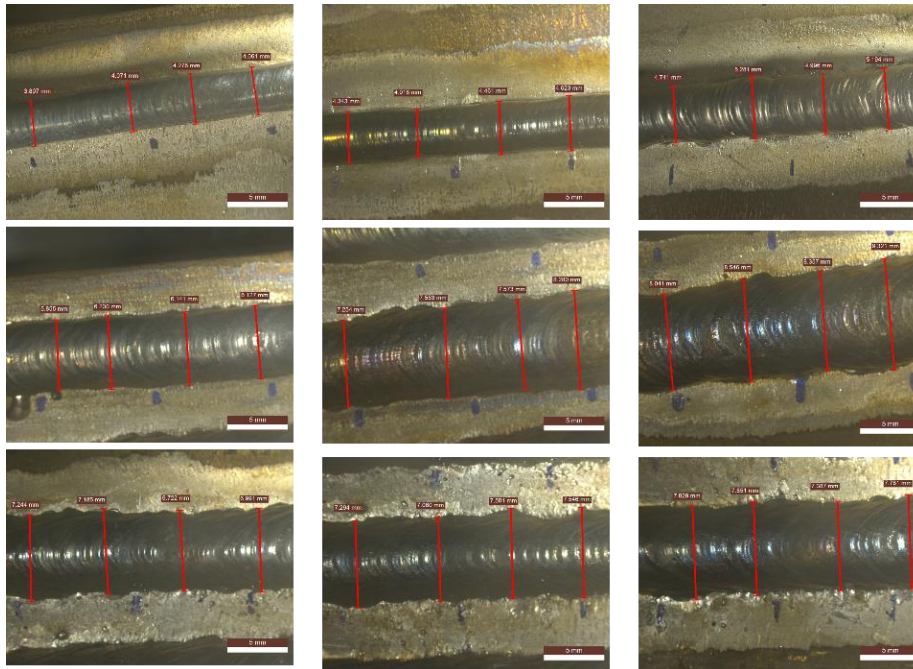


**Fig. 4.10: Track geometry analysis**

### 4.3.1 ANOVA Analysis

Anova analysis was performed on the Taguchi's L-9 model to obtain main effect plots, interaction plots, and details about how various factors influence deposition. Wire feed rate was found to be the most important parameter influencing deposition, with deposition speed and voltage coming in second and third place, respectively.

#### 4.3.1.1 Effect of voltage, wire feed rate, and deposition speed on track width

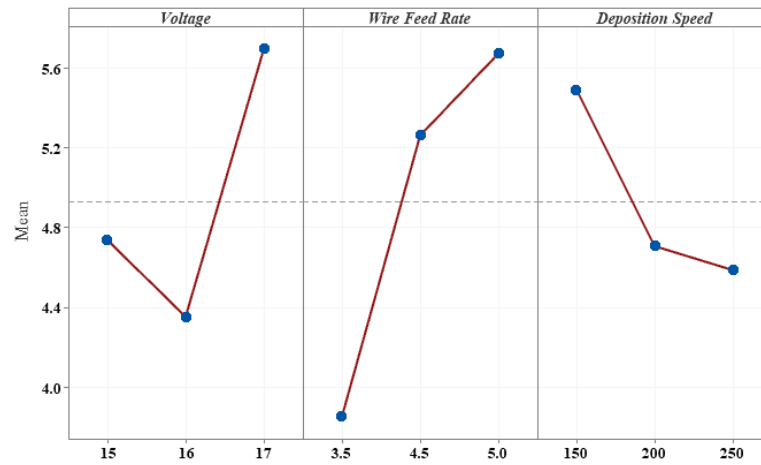


Fig. 4.11: Main Effects plot for track width

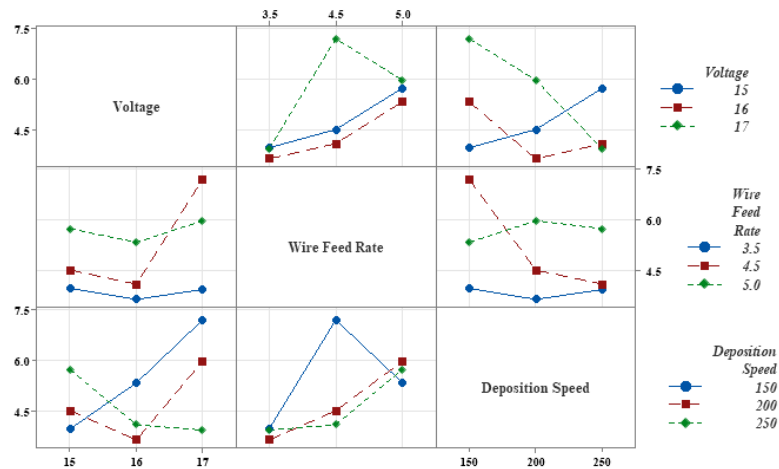


Fig. 4.12: Interaction plots for track width

Here, Fig. 4.11 depicts the variation in track width in response to variations in voltage, wire feed rate, and deposition speed. Track width was found to decrease initially, with an increase in voltage and then it starts increasing again. As the voltage increases, it results in increasing heat input into the bead, causing the temperature to rise. As a result of it, the molten material's fluidity increases and its

viscosity decreases, resulting in the molten material spreading out and therefore increasing the track width. As we increase the wire feed rate, more material goes inside the melt pool, and since the fluidity is already higher, it results in material spreading out more rapidly and hence causing the track width to increase more rapidly as compared to track height. (same can be said for increasing track height w.r.t. increasing wire feed rate). Furthermore, it was also observed that increasing the deposition speed causes a drop in track width, implying that with less speed, molten metal has more time to solidify, because of which material adheres, and track width decreases. Fig. 4.12 shows the interaction plots for track width.

#### 4.3.1.2 Effect of voltage, wire feed rate, and deposition speed on track height

Fig. 4.13 illustrates the variation of track height with respect to the changes in voltage, wire feed rate and deposition speed and fig. 4.14 shows the interaction plots for track height. Track height increases with voltage and eventually declines, in perfect contrast to track width. During the deposition, the volume deposited remains constant and since the track width increases with the increase in voltage, track height automatically decreases. Track height increases as the wire feed rate increases. The effect is comparable to that of track width, with the sole difference being the rate of increase; track width increases faster than track height. Also, it was discovered that increasing the deposition speed has a linear effect on track height.

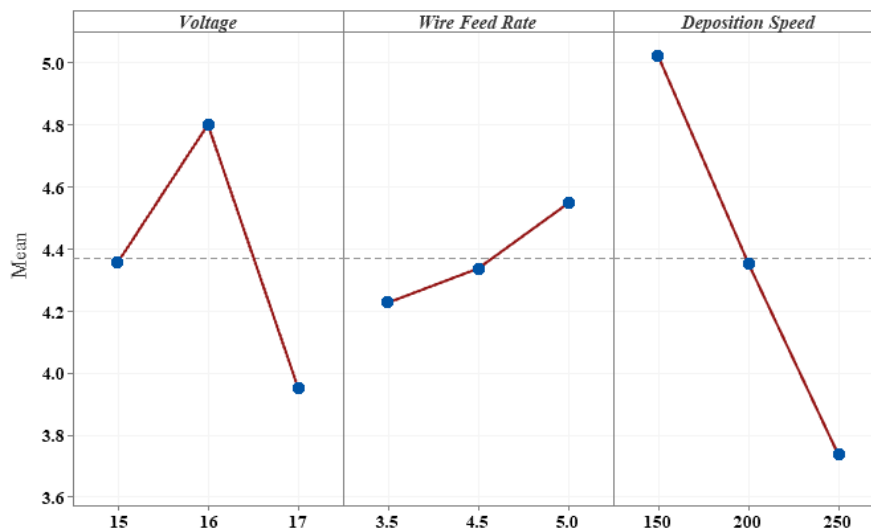


**Fig. 4.13: Main Effects plot for track height**

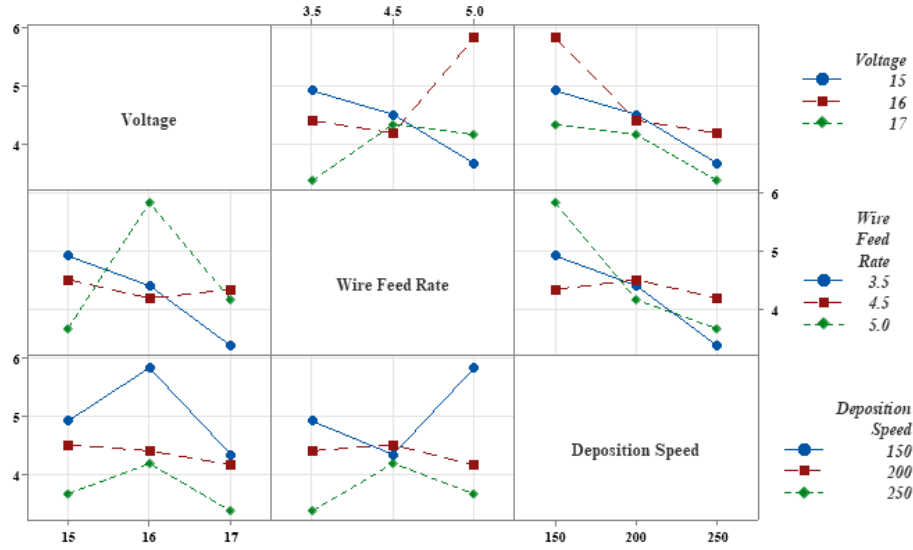


**Fig. 4.14: Interaction plots for track height**

### 4.3.2 Microstructural Analysis

Following the track geometry analysis, the aspect ratio was calculated for each parameter. Tracks with the smallest height, largest width, lowest aspect ratio, highest aspect ratio, and aspect ratio  $\approx 1$  (marked in red in table 4.6) were selected for further analysis to determine the most optimised parameter for bulk deposition. The tracks with the selected parameters were cut (shown in fig. 4.15); their microstructural and microhardness analyses were performed.

**Table 4.6: Track geometry**

Parameter	Voltage (V)	Wire feed rate(mm/min.)	Deposition Speed(mm/min.)	Track height (mm)	Track width (mm)	Aspect ratio (w/h)
1	15	3.5	150	3.97	4.91	0.80
2	15	4.5	200	4.41	4.60	0.95
3	15	5	250	5.73	3.66	1.56
4	16	3.5	200	3.65	4.40	0.82
5	16	4.5	250	4.09	4.18	0.97
6	16	5	150	5.32	5.82	0.91



7	17	3.5	250	3.94	3.25	1.21
8	17	4.5	150	7.18	4.33	1.65
9	17	5	200	5.96	4.16	1.43

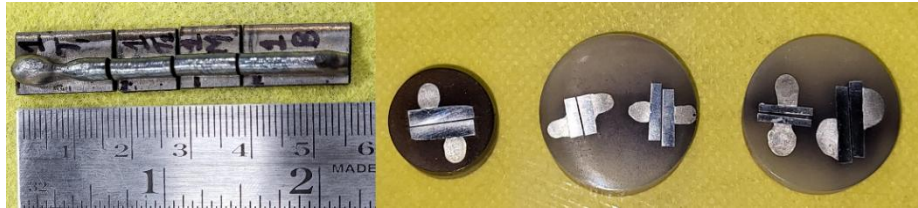


**Fig. 4.15: Cutting of single tracks and sample preparation for microstructural analysis**

Tracks at selected parameters were then cut and prepared for the microstructural analysis and their grain size was calculated using Image-J software. Fig. 4.16 and 4.17 respectively shows the microstructure and the grain size of the selected tracks.

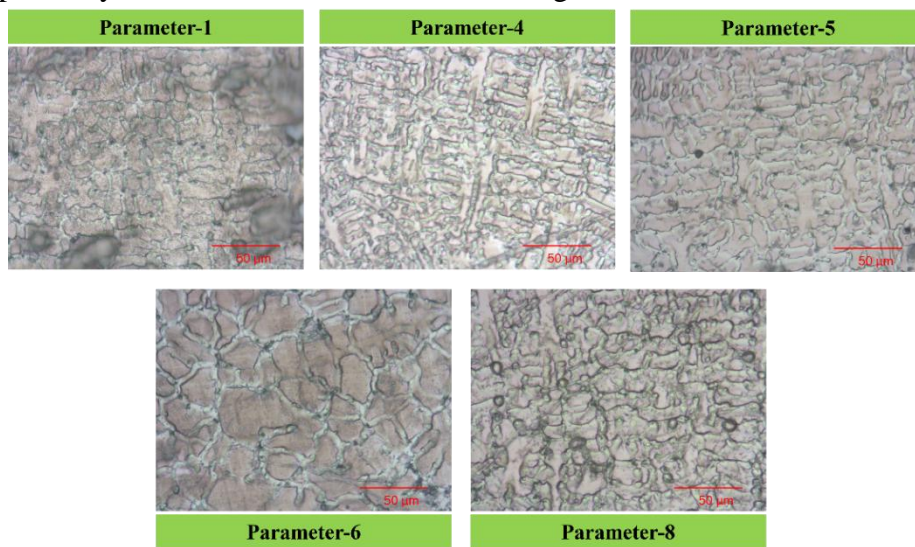


**Fig. 4.16: Microstructure of the selected tracks**

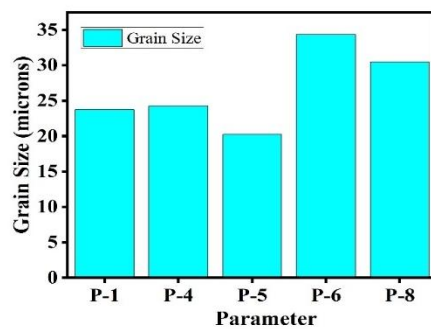


**Fig. 4.17: Grain size variation at selected parameters**

### 4.3.3 Microhardness Analysis

Vickers microhardness analysis was performed on the selected parameters. Fig. 4.18 depicts the microhardness variation across the selected parameters.

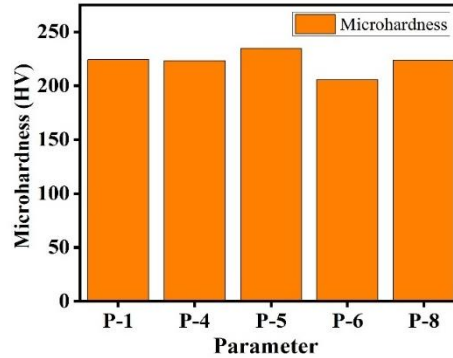


**Fig. 4.18: Microhardness variation at selected parameters**

Based on the microstructural and microhardness analysis of the selected parameters, **Parameter 5 (Voltage = 16, Wire feed rate = 4.5 and deposition speed = 250)** was considered as the best optimized parameter and was chosen for the bulk deposition.

### 4.4 Bulk Deposition

After optimizing the process parameters through initial deposition trials, bulk deposition of Inconel 617 was carried out using two distinct deposition strategies, (i.e. unidirectional and bidirectional) in the WAAM process. The objective was to evaluate the influence of deposition methodology on the build quality, microstructure, and mechanical performance of the fabricated components. The deposited samples were subjected to a comprehensive set of characterization techniques including optical and scanning electron microscopy (SEM) for microstructural analysis, Vickers microhardness testing to assess hardness distribution, tensile testing to evaluate mechanical strength, and X-ray diffraction (XRD) for phase identification. Additionally, residual stress measurements were performed to understand stress evolution within the builds. This multi-faceted analysis enabled a deeper insight into the effect of process strategies on the final properties of the WAAM-fabricated Inconel 617 components.

Two 15-layer walls measuring 30 mm in height and 60 mm in length were deposited by different deposition strategies. Figure 4.19 depicts the schematic and wall deposited using a bidirectional strategy, whereas Figure 4.20 depicts the schematic and wall deposited using a unidirectional strategy.

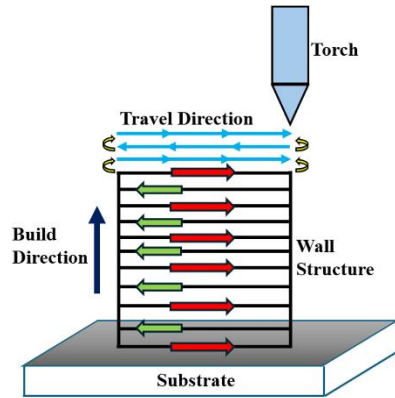


**Fig. 4.19: Bidirectional deposition strategy schematic(left) and deposited wall(right)**

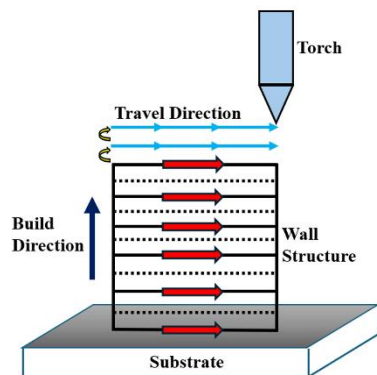


**Fig. 4.20: Unidirectional deposition strategy schematic(left) and deposited wall(right)**

#### 4.4.1 Microstructural Analysis

The deposited walls were then cut along their cross section in the built direction with a wire EDM machine, and their microstructural properties were examined. Microstructures were revealed through electrolytic etching at 6 V for 10-60 seconds with a 10% oxalic acid solution as an etchant, and microstructural images were captured using an inverted microscope. Figure 4.21 depicts the cross section and microstructural features of the as deposited wall using a bidirectional strategy along the building direction, while Figure 4.22 depicts the cross section and

microstructural features of the as deposited wall using a unidirectional strategy along the building direction.

#### **4.4.1.1 Bidirectional Deposition Strategy**

Fig. 4.21(c) shows microstructural properties of the bottom layers, which demonstrate the presence of cellular and equiaxed grains. Variations in the microstructure along the building direction can be attributed to changes in cooling rates as we ascend upwards along the building direction[26]. During the deposition of initial layers, heat generated during the deposition gets dissipated easily through the substrate, thus resulting in finer grain structure as compared to subsequent layers. Fig. 4.21(b) illustrates the microstructure in the middle layers of the deposition. Like the bottom layers, cellular and equiaxed grains were more prevalent in the middle layers also. Although the grain size was larger than that in the bottom layers, this was due to the slower cooling rate in the middle layers. Because of the subsequent deposition of layers on top of one another, heat generated during the deposition of the middle layers is not easily distributed, as the bottom layers are already hot. This causes an increase in grain size in the middle layers. Fig. 4.21(a) represents the microstructure of the upper layers. Heat generated gets dissipated into the environment via convection and into prior layers via conduction, resulting in finer grains than in middle layers.

#### **4.4.1.2 Unidirectional Deposition Strategy**

For the unidirectional strategy, it was observed that at the bottom of the deposition, cellular grains were observed, as depicted in fig. 4.22(c), which can be attributed to the faster cooling rate through the substrate. As we move upward in the build direction, it was observed that the grain size increases gradually till the top of deposition, it was observed that the columnar grains start forming as we go towards the top, as depicted in fig. 4.22(b) and 4.22(a). The variation in the grain size can be attributed to the progressive accumulation of heat along the same travel direction during successive layers. As each new layer is deposited in the same direction, the previously deposited layers retain heat due to the reduced inter-layer cooling time, resulting in a gradual increase in the overall thermal gradient and substrate



temperature. This thermal buildup causes a lower cooling rate at higher layers, which promotes grain coarsening and leads to a continuous increase in grain size. In contrast, the bidirectional strategy alternates the deposition direction with each pass, which redistributes the heat more evenly across the wall. This alternating pattern helps in breaking the thermal accumulation pattern and introduces more uniform cooling across layers. Fig. 4.23 depicts the variation in the grain size in both the deposition strategies.

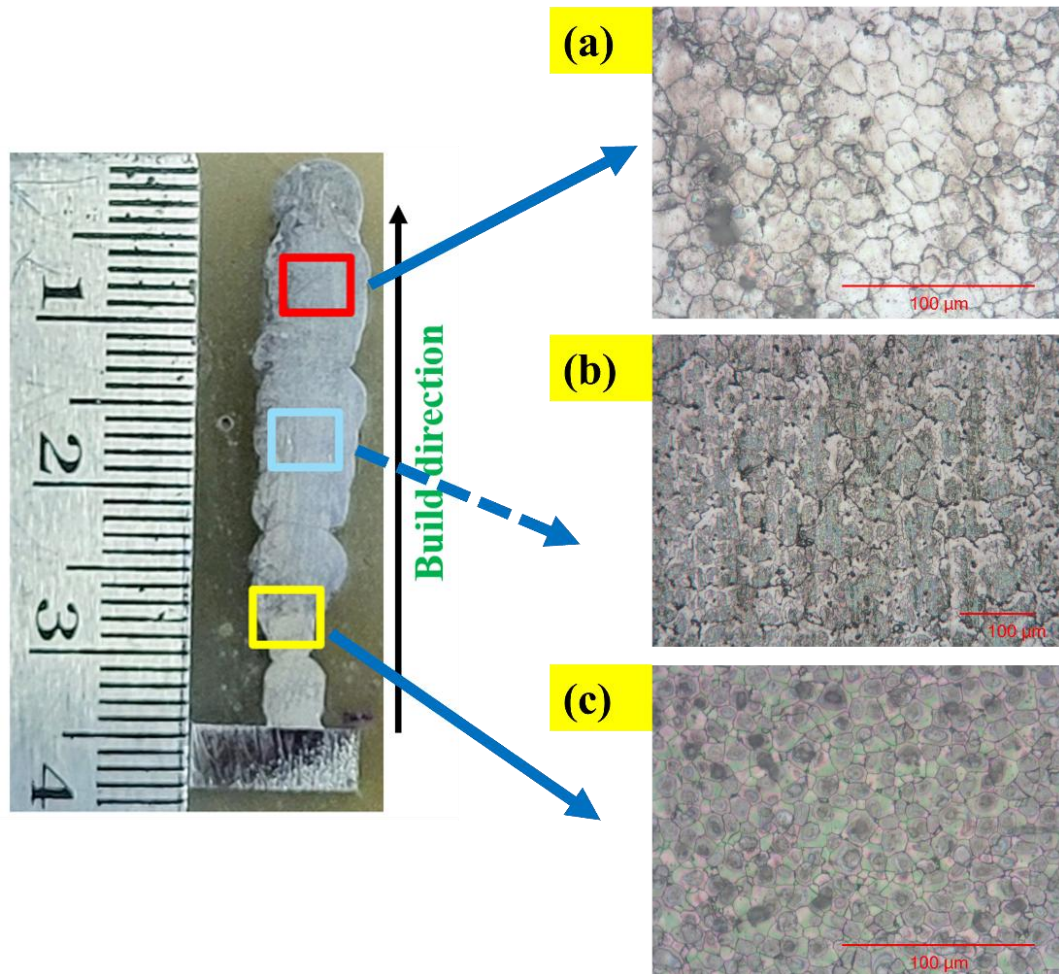


**Fig. 4.21: Microstructure variation across layers in bidirectional strategy**

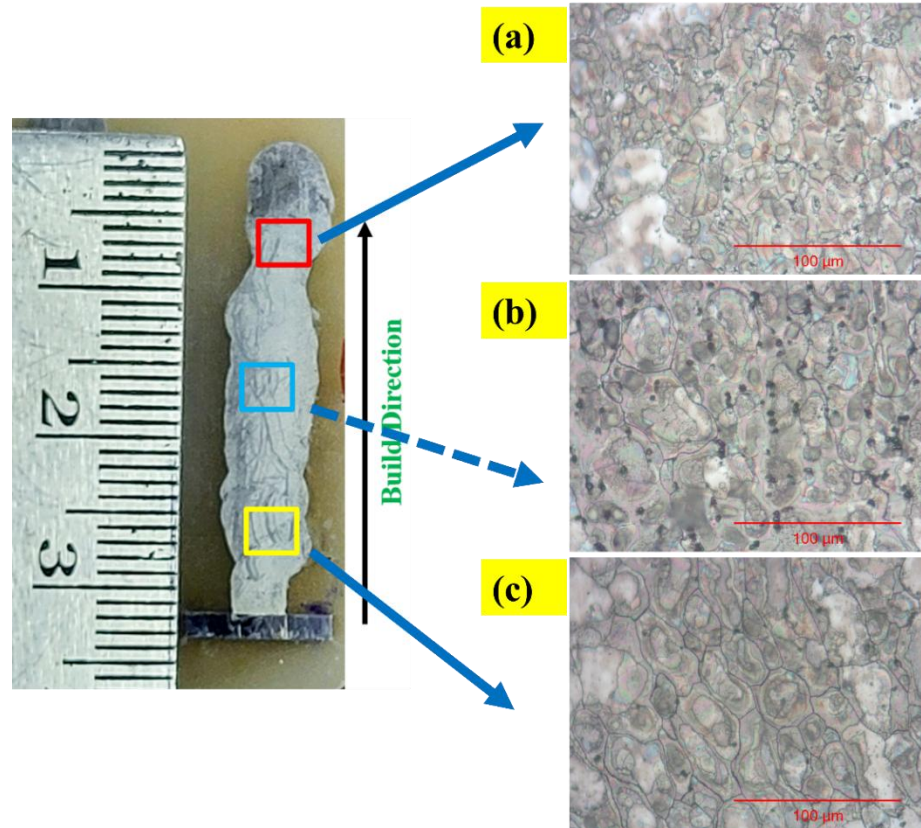


**Fig. 4.22: Microstructure variation across layers in unidirectional strategy**

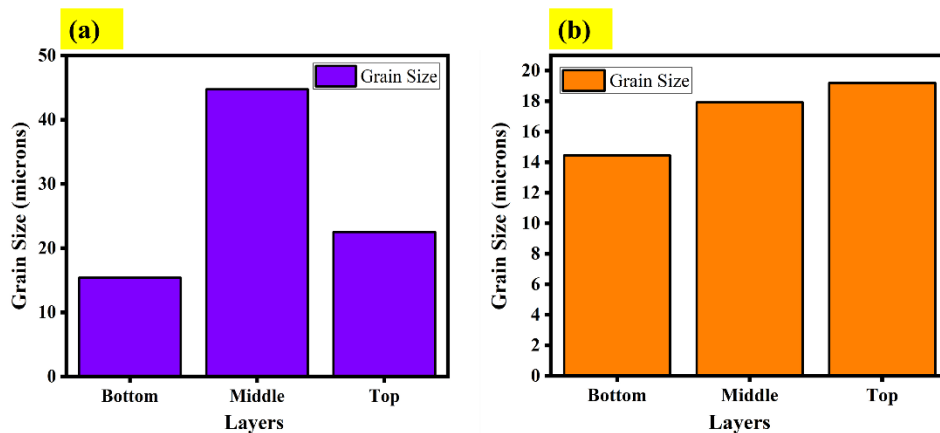
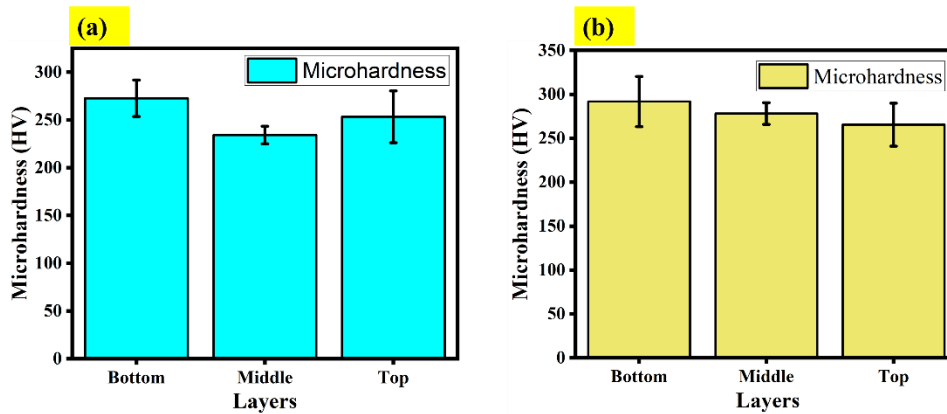


**Fig. 4.23: Grain size variation across layers in (a) bidirectional strategy and (b) unidirectional strategy**

#### 4.4.2 Microhardness Analysis

Figure 4.24 depicts the variation in microhardness across three zones (bottom, middle, and top) along the building direction in bidirectional and unidirectional strategies respectively. The Vickers microhardness method was used in the testing

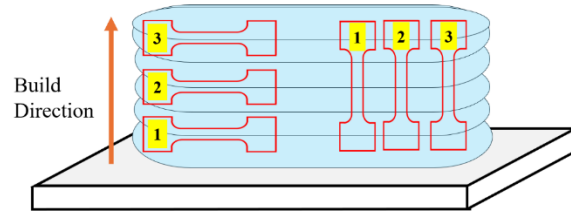
because of its accuracy in measuring minute differences in hardness across different microstructural regions. Indentations were made with a 0.2 kgf (1.96 N) load with a dwell time of 10 seconds. For the bidirectional strategy, as depicted in fig. 4.24(a), the microhardness value is highest at the bottom, gradually lowering towards the middle, and then increasing again towards the top. The variation in microhardness across different zones can be attributed to both grain size and cooling rate. Bottom layers had the smallest grain size due to the rapid cooling rate, which contributed to their high microhardness value. Similarly, as we move upwards, high grain size in the middle layers results in the lowest microhardness value, and as we move towards the upper zone, cooling rate in the upper layers improves as compared to the middle zone, resulting in finer grains and a higher microhardness value than the middle zone. In unidirectional strategy, it was observed that with accordance to the grain size variation, microhardness value was highest at the bottom and decreases as we move towards the top. Fig. 4.24(b) depicts the microhardness variation in the unidirectional strategy.



**Fig. 4.24: Microhardness variation in in (a) bidirectional strategy and (b) unidirectional strategy**

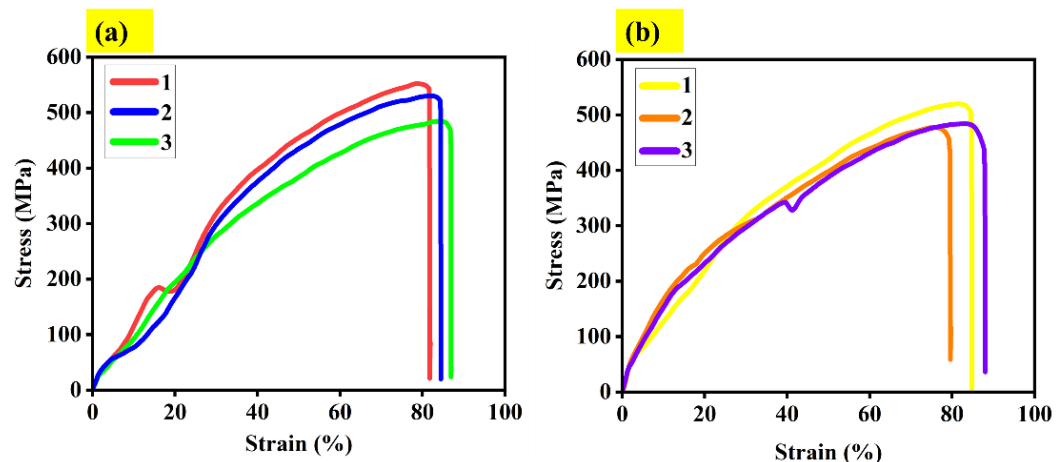
#### 4.4.3 Tensile Test

Fig. 4.25 shows the schematic according to which the micro-tensile samples were cut for analysing the tensile properties of the Inconel 617 alloy. Three specimens each were cut in horizontal and vertical orientation to know the influence of the deposition strategies in different directions.



**Fig. 4.25: Schematic for micro tensile test**

The samples were tested at a constant strain rate of 10 mm/min and their tensile properties, i.e. tensile stress or ultimate tensile strength, yield strength and elongation at break are calculated. Tensile testing was performed on samples extracted from both bidirectional and unidirectionally deposited Inconel 617 walls, with specimens orientated horizontally and vertically relative to the build axis. The results consistently showed that the horizontal orientation samples had a higher tensile strength than the vertical ones, regardless of the deposition strategy used. This trend is attributed to the anisotropic microstructure inherent in the wire arc additive manufacturing (WAAM) process. Consequently, samples tested in the vertical orientation are more susceptible to failure along these interlayer regions, which often act as sites of weakness due to incomplete fusion or residual stress accumulation. In contrast, horizontally oriented specimens benefit from a more continuous metallic matrix, resulting in superior tensile properties. These findings highlight the significant impact of build orientation on the mechanical performance of WAAM-fabricated components, emphasising the importance of considering orientation effects during component design and process optimisation. Figs. 4.26 and 4.27 represents the stress-strain curves for the bidirectional and unidirectional strategies respectively.



**Fig. 4.26: Tensile test results for bidirectional deposition; (a) horizontal orientation and (b) vertical orientation**

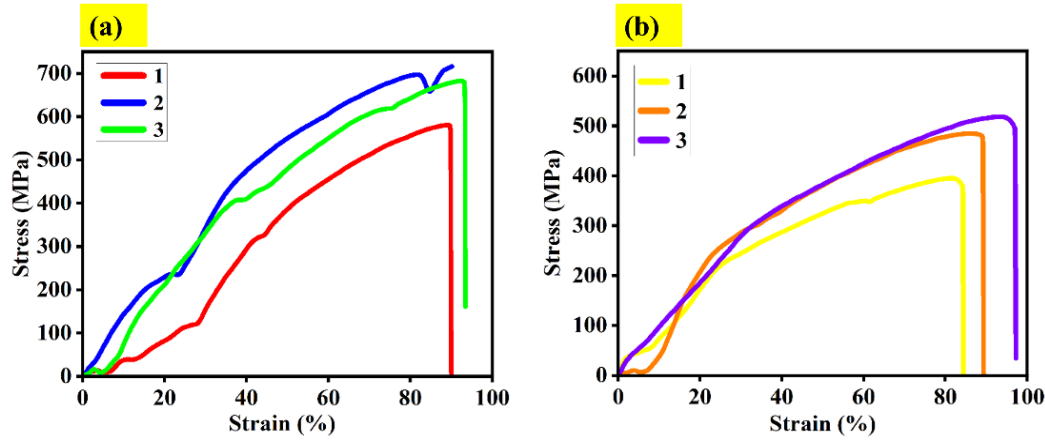


**Fig. 4.27: Tensile test results for unidirectional deposition; (a) horizontal orientation and (b) vertical orientation**

According to ASTM B168-19, the average tensile properties of Inconel 617 are Ultimate Tensile Strength=655 MPa, Elongation=35% and Yield Stress=240 MPa [26]. The average elongation and yield stress of the WAAM deposited samples were quite higher than the ASTM B168-19 standards and the ultimate tensile strength was consistent with the ASTM standard. Table 4.7 and 4.8 illustrates the tensile test results for bidirectional and unidirectional strategies respectively.

**Table 4.7: Tensile test results for bidirectional strategy**

	Measured Value (Horizontal orientation)	Measured Value (Vertical orientation)
<b>Ultimate Tensile Strength</b>	522.06 ± 34.50 MPa	493.68 ± 22.94 MPa
<b>Yield Stress</b>	389.11 ± 40.12 MPa	337.21 ± 29.88 MPa
<b>Elongation</b>	84.43 ± 2.54%	84.17 ± 4.17%

**Table 4.8: Tensile test results for unidirectional strategy**

	<b>Measured Value (Horizontal orientation)</b>	<b>Measured Value (Vertical orientation)</b>
<b>Ultimate Tensile Strength</b>	670.76 ± 85.73 MPa	462.52 ± 63.40 MPa
<b>Yield Stress</b>	260.20 ± 56.65 MPa	296.04 ± 20.56 MPa
<b>Elongation</b>	94.83 ± 6.06%	88.97 ± 6.10%

Following the tensile test, fractography analysis of the fractured samples was performed to determine the mode of failure. The mode of failure was found to be predominantly ductile in all samples. Horizontally orientated samples from both deposition strategies exhibit consistent dimple formation, as illustrated in figs. 4.28(a) and 4.28(c), which represent ductile failure. Vertically orientated samples, on the other hand, formed shear bands, fibrous texture, and dimples, as shown in figs. 4.28(b) and 4.28(d), respectively. Because of the microstructural inhomogeneity in the vertically orientated samples, certain regions experienced intense shearing from the combined effects of tensile and shear stresses, resulting in the formation of shear bands. Fibrous texture, on the other hand, indicates that the material was subjected to plastic deformation prior to separation or fracture.



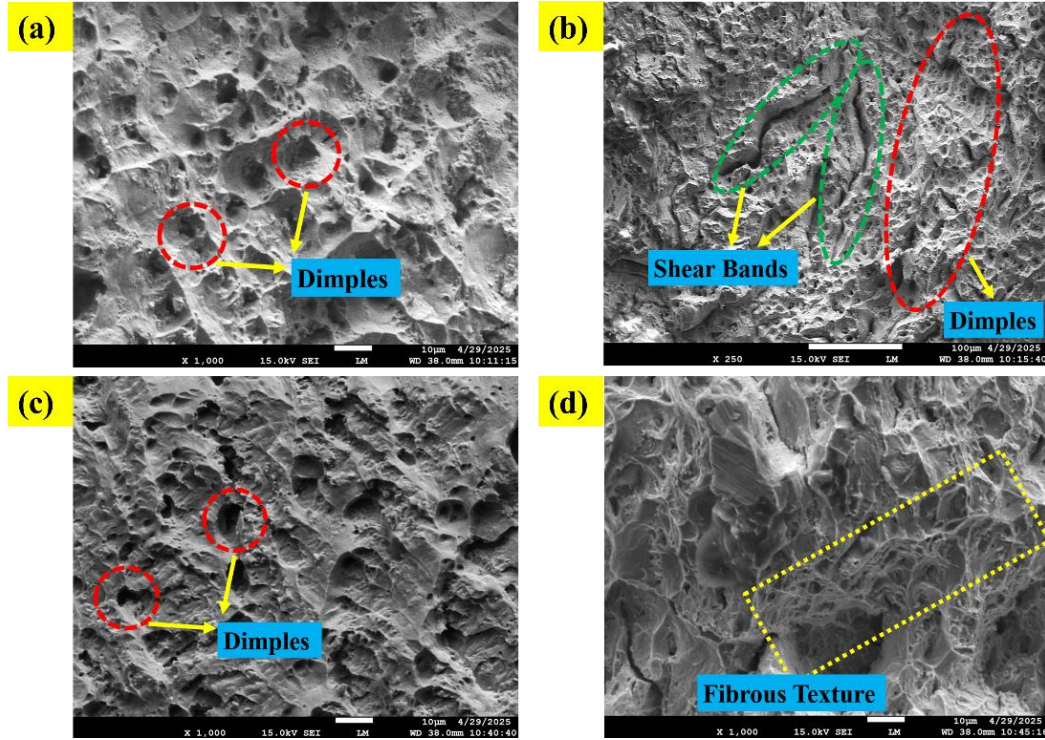


**Fig. 4.28: Fractography images for; (a) horizontally oriented specimen using bidirectional strategy, (b) vertically oriented specimen using bidirectional strategy, (c) horizontally oriented specimen using unidirectional strategy, (d) vertically oriented specimen using unidirectional strategy**

#### 4.4.4 XRD Analysis

The deposited samples were then characterized using the XRD analysis. Normal XRD scans were done throughout a  $2\theta$  range of  $10^0$  to  $90^0$ . X-ray diffraction (XRD) was performed on Inconel 617 walls deposited using both bidirectional and unidirectional WAAM strategies, with samples extracted from the bottom (B-B), middle (B-M), and top (B-T) regions and were examined for phases and peak positions. Fig. 4.29 depicts the XRD patterns for the WAAM deposited Inconel 617 alloy. XRD peaks with corresponding planes are identified as (111), (200), and (220). All of these belong to the FCC lattice[30]. All patterns exhibit prominent peaks corresponding to the  $\gamma$ -Ni FCC phase at (111), (200), and (220) planes, indicating a single-phase structure. The unidirectional sample has significantly higher peak intensities at the base, indicating strong crystallographic texture caused by heat accumulation and slower cooling. In contrast, the bidirectional sample

exhibits more evenly distributed intensities, indicating more uniform grain growth. These variations are due to differences in thermal gradients and heat input distribution between the two deposition strategies.

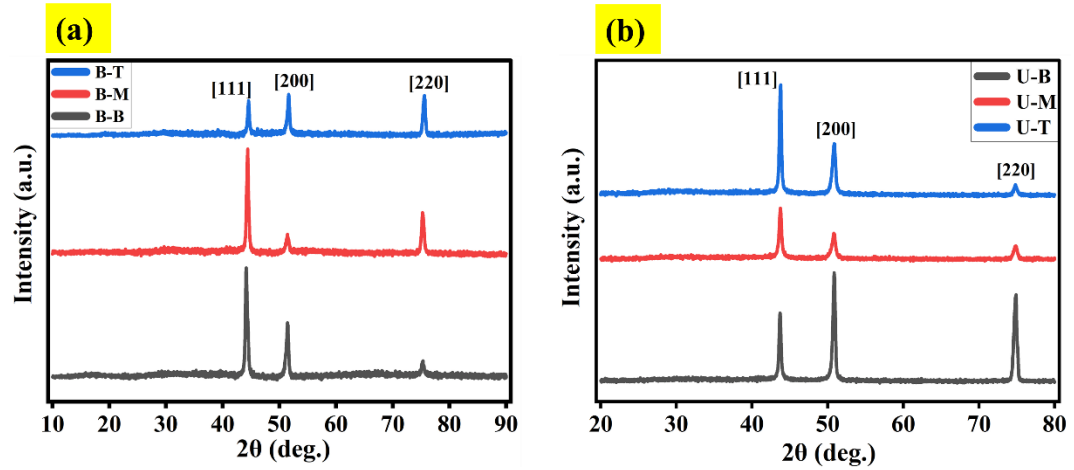


**Fig. 4.29: XRD patterns for WAAM deposited In-617; (a) bidirectional strategy, (b) unidirectional strategy**

#### 4.4.5 Residual Stress Analysis

For residual stress analysis, an XRD scan at  $74.83^\circ$  (220 peak) for seven different tilt angles ( $\psi$ ) is performed and residual stress value was calculated using **d-spacing vs  $\sin^2\psi$**  method. The formula used for residual stress calculation is:

$$\sigma = \frac{E}{1+\nu} \cdot \frac{1}{d_0} \cdot m \dots\dots\dots(1)$$

Here,  $\sigma$  = Residual stress,  $E$  = Young's Modulus,  $\nu$  = Poisson's ratio,

$d_0$  = d-spacing at  $\psi = 0$ ,  $m$  = slope of d-spacing vs  $\sin^2\psi$  plot and

$\Psi$  = tilt angle

In the bidirectional deposition, compressive residual stresses were observed at the top ( $-4.11$  GPa) and bottom ( $-1.04$  GPa), while a high tensile stress was recorded in the middle region ( $6.37$  GPa). This can be attributed to in bidirectional deposition, alternating scan directions promote more uniform heat distribution, reducing localised thermal gradients and allowing partial stress relaxation through thermal cycling[40], [41]. For unidirectional deposition, consistent travel direction causes asymmetric heat accumulation, resulting in higher thermal gradients. This causes



tensile stresses at the top (2.57 GPa) and bottom (4.31 GPa) due to rapid solidification shrinkage near the substrate interface and free surface[40], [41], while the middle region develops compressive stress (-3.42 GPa) due to stress reversal from accumulated plastic strain during cyclic heating[42]. These findings underscore the importance of deposition strategy in controlling residual stress profiles in WAAM processes, which is critical for ensuring dimensional stability and mechanical integrity in high-temperature applications. Figs. 4.30 and 4.31 show the linear fit plots for calculating the slope(m) for the bidirectional and unidirectional depositions, which are being used in equation 1 for calculating residual stresses.

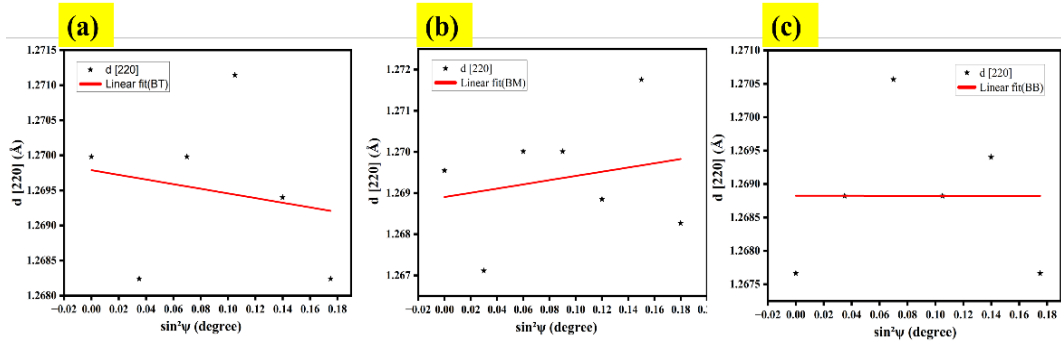


**Fig. 4.30: Linear fit plots for bidirectional strategy; (a) top, (middle) and (c) bottom**

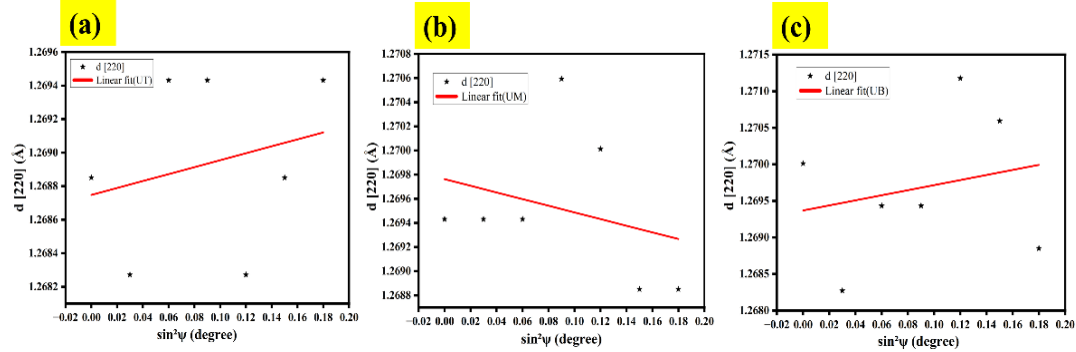


**Fig. 4.31: Linear fit plots for unidirectional strategy; (a) top, (middle) and (c) bottom**

#### 4.5 In-situ Monitoring of WAAM Deposition

In this study, we have employed a novel technique of Time Resolved Reflectivity (TRR) for real time monitoring of the WAAM process to study the melt pool behaviour as well as discontinuity detection during the deposition. It is a technique

that monitors changes in reflectivity over time. It measures how the reflectivity of a material changes as a function of time, allowing to study dynamic processes, occurring within the material. When a laser beam is directed at a sample, the reflected light intensity is monitored over time. Changes in the reflectivity are correlated with the interface movement, temperature, or other relevant changes occurring within the sample. Fig. 4.32 shows the schematic for TRR.

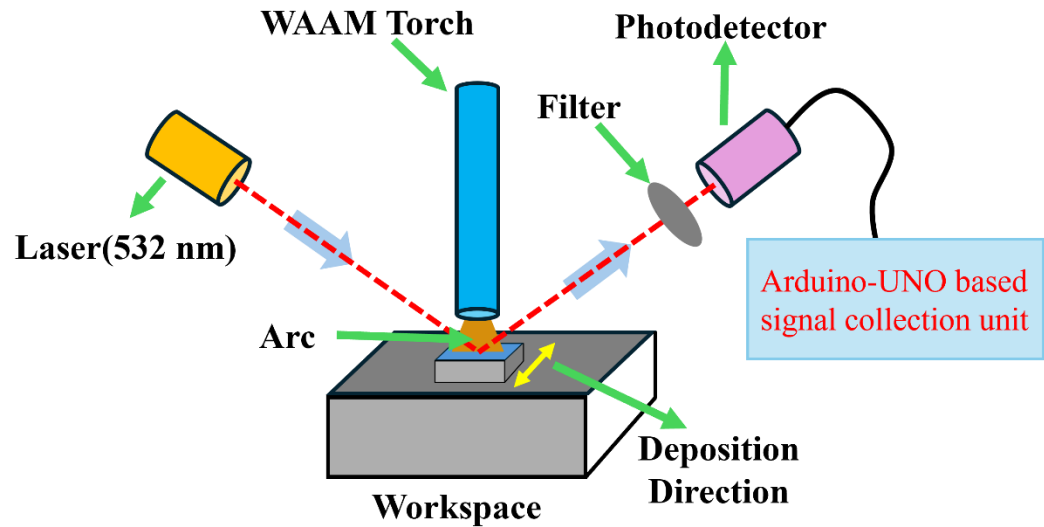


**Fig. 4.32: Schematic for TRR**

The reflected intensity varies with the phase change; when it is high, it is referred to as a melting region, and when it is low, it is referred to as a vaporisation region. In the TRR setup, a filter was placed in front of the photodetector to reduce errors caused by WAAM spattering and ambient light. This eliminated noise and enabled more precise readings. Only reflected light with a wavelength of 532 nm will pass through this filter and be detected by the photodiode. To assess the effect of using the filter during deposition, experiments were performed with and without the filter, and it was discovered that when the filter was not present, the photodetector acquired noise along with the reflected signal intensity, whereas with the filter, more accurate and precise results were obtained, as shown in fig. 4.33. Fig. 4.33(b) clearly illustrates that when the filter was not there, a lot of noise was there, as compared to the fig. 4.33(a).

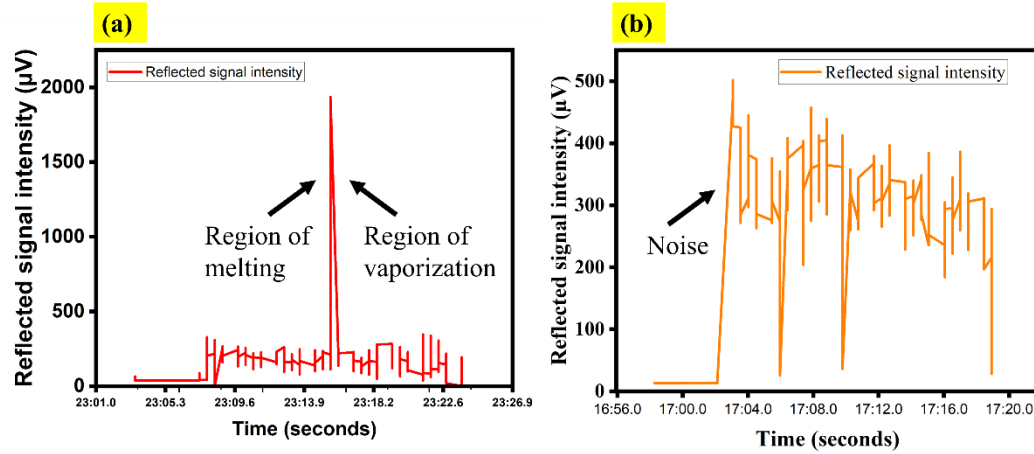


**Fig. 4.33: Reflected signal intensity measurement; (a) with filter, (b) without filter**

#### 4.5.1 Discontinuity Detection using TRR

During the initial phase of the study, Time-Resolved Reflectivity (TRR) was used as an in-situ monitoring technique to identify and indicate discontinuities in the Wire Arc Additive Manufacturing (WAAM) process. TRR detects changes in the intensity of light reflected from a molten pool or recently solidified surface. During stable and uniform deposition, the melt pool surface is relatively smooth and consistent, resulting in minimal variation in reflected signal intensity. However, any fluctuations in process stability, such as porosity formation, lack of fusion, uneven layer height, or other discontinuities, can cause changes in surface morphology and temperature gradients, which will have a direct impact on reflectivity. These deviations appear as sharp changes or fluctuations in the TRR signal. Continuously recording the reflected intensity over time and plotting it against the deposition time or layer number allows you to see where anomalies or defects may have occurred. This makes TRR an effective tool for real-time defect detection and quality assurance in WAAM, allowing for early intervention and possible process correction. Furthermore, its non-intrusive nature and sensitivity to surface condition make it highly appropriate for integration into automated monitoring frameworks in additive manufacturing processes. Fig. 4.34 represents the discontinuity detection using TRR.

Fig. 4.34(a) shows a series of discrete and irregular beads, each with varying sizes and spacings. The corresponding TRR signal displays frequent and sharp drops in reflected signal intensity. These fluctuations are indicative of significant variations in melt pool dynamics during deposition. The sudden dips in the reflected signal can be attributed to rapid changes in melt pool size and surface morphology, possibly due to inconsistent heat input, unstable wire feed, or lack of synchronization between process parameters. The non-uniform bead formation suggests that the process was operating in a pulsed or intermittent mode, where the arc was frequently extinguished or repositioned, leading to inconsistent remelting and cooling. This resulted in high reflectivity variance, captured in the TRR signal as sharp peaks and troughs.

Fig. 4.34(b), in contrast, shows a continuous and uniform bead with a consistent width and smooth surface morphology. The associated TRR signal is comparatively stable, with only a few initial disturbances followed by a steady pattern with minor fluctuations. This indicates that the melt pool remained relatively consistent throughout the deposition process. The initial dip in the signal could correspond to the start of deposition, during which thermal equilibrium and stable arc formation are being established. Once the process stabilizes, the reflected intensity remains high and steady, suggesting minimal disturbance in the melt pool surface and consistent energy absorption. The uniformity in the bead corroborates this, showing that optimized parameters and stable wire feeding likely contributed to continuous and defect-free deposition.

In summary, the TRR signal effectively captures the real-time dynamics of the melt pool. The unstable signal in fig. 4.34(a) corresponds to non-uniform bead formation, indicating poor process stability. In contrast, the smoother signal in fig. 4.34(b) aligns with uniform bead geometry, reflecting better thermal and process control.

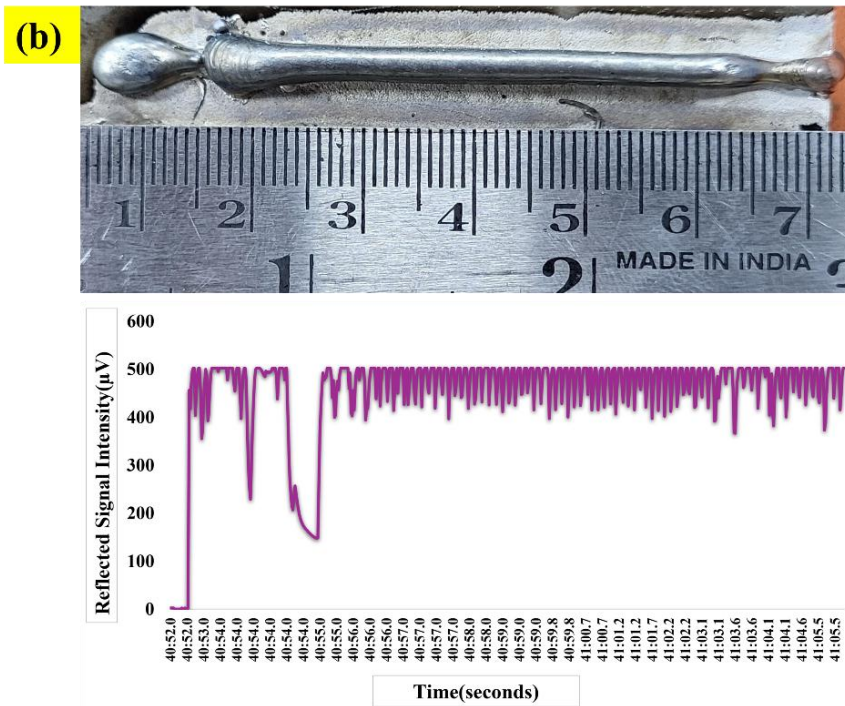
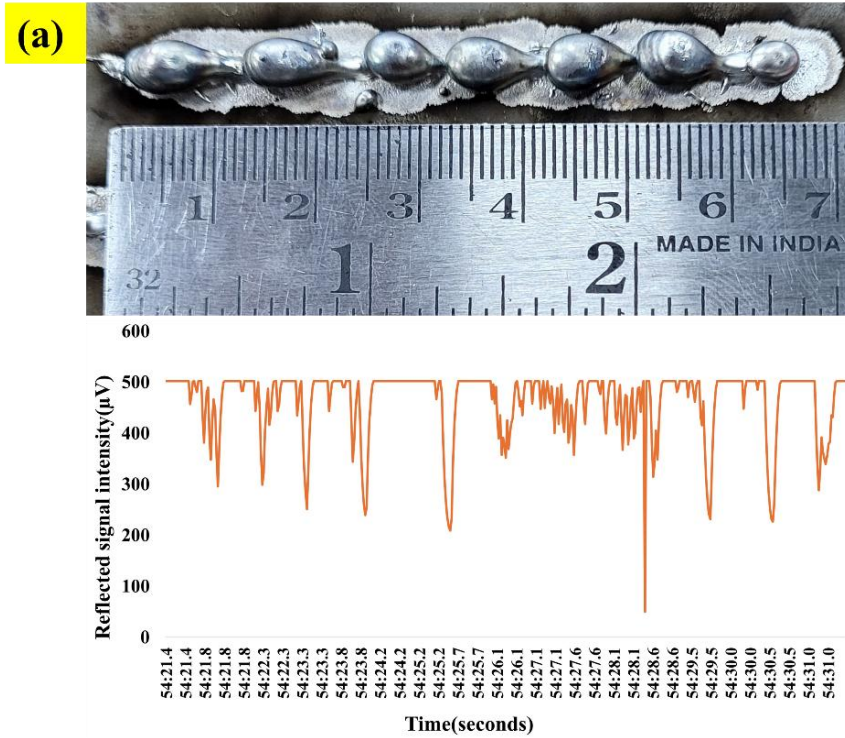


**Fig. 4.34(a & b): Discontinuity detection using TRR; graph for the respective bead is plotted against it, which shows the fluctuations whenever a discontinuity is occurring**

## Chapter 5

---

### Conclusions and Future Scope

This chapter summarizes the key findings of the present work and highlights the major conclusions drawn from the experimental investigations. It reflects on how the objectives of the study were achieved and discusses the implications of the results in the broader context of additive manufacturing. Additionally, potential areas for future research are outlined, focusing on improving process stability, enhancing material properties, and expanding the scope of in-situ monitoring techniques for advanced manufacturing applications.

#### 5.1 Conclusions

The following conclusions can be made from the work presented in this thesis:

- The research successfully demonstrated the fabrication of Inconel 617 using two additive manufacturing techniques: Laser Additive Manufacturing - Directed Energy Deposition (LAM-DED) and Wire Arc Additive Manufacturing (WAAM).
- Preliminary trials using LAM-DED successfully demonstrated the feasibility of fabricating Inconel 617 with good control over track geometry and microstructure.
- Based on various pilot experiments on LAM-DED, process parameters for deposition were chosen and these process parameters, i.e. laser power and scan speed were systematically varied while maintaining a constant powder feed rate.
- Laser Power was varied in two different levels, i.e. 650 W and 750 W. Scan speed was varied in three different levels, i.e. 600, 700 and 800 mm/min.
- LAM-DED produced a heterogeneous microstructure with equiaxed grains in bottom layers and columnar grains in upper layers, attributed to varying cooling rates during layer-by-layer deposition.

- Microhardness measurements in LAM-DED deposited sample indicated higher hardness in bottom layers (due to fine equiaxed grains) and lower hardness in upper layers (due to coarse columnar grains), confirming the influence of cooling rate and grain structure.
- LAM-DED samples showed an average ultimate tensile strength (UTS) of 381.78 MPa, lower than ASTM B168-19 standards (655 MPa), likely due to inter-dendritic segregations and cracking susceptibility.
- Despite the reduced UTS in LAM-DED deposited sample, the elongation (31.3%) and yield strength (202 MPa) were reasonably close to standard requirements, indicating potential for further optimization.
- WAAM was chosen as the primary method for further investigations due to its high deposition rate, better material utilization, and lower operational costs, especially when using wire feedstock.
- Extensive parameter optimization was carried out using a structured Taguchi's L9 orthogonal array design, varying voltage, wire feed rate, and deposition speed.
- ANOVA analysis for WAAM deposited samples identified wire feed rate as the most significant parameter affecting track geometry, followed by deposition speed and voltage.
- In single track analysis, it was found that track width and track height increase with an increase in wire feed rate and decrease with an increase in deposition speed.
- Based on the process parameter optimization, **Parameter 5, i.e. Voltage =16V, Wire Feed Rate =4.5m/min., and Deposition Speed = 250 mm/min** was decided as the most optimized parameter for bulk deposition on WAAM.
- WAAM deposition was performed using two strategies, i.e. bidirectional and unidirectional.
- In both bidirectional and unidirectional strategies, grain structure evolves along the build direction due to varying cooling rates.

- The bidirectional deposition strategy results in relatively uniform grain structure across bottom, middle, and top layers. This is due to alternating heat flow and more balanced thermal distribution, which mitigates excessive thermal buildup.
- In the unidirectional strategy, continuous deposition in the same direction results in progressive heat build-up, particularly in higher layers, leading to coarser grain growth and the eventual formation of columnar grains at the top.
- The microhardness results show that the microhardness in the bidirectional strategy was 272.72 HV (bottom), 234.31 HV (middle), and 253.30 HV (top), whereas the values in the unidirectional strategy were 291.76 HV (bottom), 278.13 HV (middle), and 265.42 HV (top).
- Tensile results show that the UTS values in the bidirectional strategy were  $522.06 \pm 34.50$  MPa for horizontal orientation and  $493.68 \pm 22.94$  MPa for vertical orientation.
- Tensile results show that the UTS values in the unidirectional strategy were  $670.76 \pm 85.73$  MPa for horizontal orientation and  $462.52 \pm 63.40$  MPa for vertical orientation.
- Fractography analysis shows that the mode of failure in tensile test was predominantly ductile.
- XRD analysis revealed the formation of three peaks at [111], [200] and [220] at angles nearly equal to 430, 510 and 750. Presence of single phase is confirmed, i.e.  $\gamma$  – Ni (FCC).
- Residual Stress analysis shows that in bidirectional deposition strategy, top and bottom regions experience compressive residual stresses, while the middle region experiences tensile residual stresses and in Unidirectional deposition strategy, top and bottom regions experience tensile residual stresses, while the middle region experiences compressive residual stresses.
- Time resolved reflectivity(TRR) can be employed in in-situ monitoring as well as for Discontinuity Detection during the deposition.



## **5.2 Future Scope**

Based on the conclusions obtained from the study, the work done can be explored in various other ways. The future scope of the work includes:

- Closed – loop feedback system based on TRR can be integrated with WAAM.
- Multi-layer depositions can be performed with in-situ corrections.
- Laser post processing techniques such as laser shock peening and laser annealing can be explored for residual stress management.
- AM deposited parts can be built for functional applications in high temperature applications.

## REFERENCES

- [1] C.P. Paul and A.N. Jinoop, *Additive Manufacturing: Principles, Technologies and Applications*, 1st ed. McGraw Hill Education. , 2021.
- [2] A. Al Rashid, S. A. Khan, S. G. Al-Ghamdi, and M. Koç, “Additive manufacturing: Technology, applications, markets, and opportunities for the built environment,” Oct. 01, 2020, *Elsevier B.V.* doi: 10.1016/j.autcon.2020.103268.
- [3] S. Yadav, & A. N. Jinoop, N. Sinha, C. P. Paul, and K. S. Bindra, “Parametric investigation and characterization of laser directed energy deposited copper-nickel graded layers”, doi: 10.1007/s00170-020-05644-9/Published.
- [4] D. G. Ahn, “Directed Energy Deposition (DED) Process: State of the Art,” Mar. 01, 2021, *Korean Society for Precision Engineering*. doi: 10.1007/s40684-020-00302-7.
- [5] A. N. Jinoop, C. P. Paul, and K. S. Bindra, “Laser-assisted directed energy deposition of nickel super alloys: A review,” Nov. 01, 2019, *SAGE Publications Ltd.* doi: 10.1177/1464420719852658.
- [6] A. L. B. Novelino, G. C. Carvalho, and M. Ziberov, “Influence of WAAM-CMT deposition parameters on wall geometry,” *Advances in Industrial and Manufacturing Engineering*, vol. 5, Nov. 2022, doi: 10.1016/j.aime.2022.100105.
- [7] D. Jafari, T. H. J. Vaneker, and I. Gibson, “Wire and arc additive manufacturing: Opportunities and challenges to control the quality and accuracy of manufactured parts,” *Mater Des*, vol. 202, Apr. 2021, doi: 10.1016/j.matdes.2021.109471.
- [8] K. Treutler and V. Wesling, “The current state of research of wire arc additive manufacturing (Waam): A review,” Sep. 01, 2021, *MDPI*. doi: 10.3390/app11188619.
- [9] C. R. Cunningham, J. M. Flynn, A. Shokrani, V. Dhokia, and S. T. Newman, “Invited review article: Strategies and processes for high quality wire arc additive manufacturing,” Aug. 01, 2018, *Elsevier B.V.* doi: 10.1016/j.addma.2018.06.020.
- [10] D. Ding, Z. Pan, D. Cuiuri, and H. Li, “Wire-feed additive manufacturing of metal components: technologies, developments and future interests,” Oct. 26, 2015, *Springer London*. doi: 10.1007/s00170-015-7077-3.
- [11] M. Grasso and B. M. Colosimo, “Process defects and in situ monitoring methods in metal powder bed fusion: A review,” Apr. 01, 2017, *Institute of Physics Publishing*. doi: 10.1088/1361-6501/aa5c4f.

- [12] T. Craeghs, S. Clijsters, J. P. Kruth, F. Bechmann, and M. C. Ebert, "Detection of Process Failures in Layerwise Laser Melting with Optical Process Monitoring," in *Physics Procedia*, Elsevier B.V., 2012, pp. 753–759. doi: 10.1016/j.phpro.2012.10.097.
- [13] T. C. S. Y. E. Craeghs, "Online Quality Control of Selective Laser Melting," University of Texas at Austin.
- [14] D. H. Lowndes; R. F. Wood, "Time-resolved reflectivity during pulsed-laser irradiation of GaAs," *Appl. Phys. Lett.* , vol. 38, no. 12, Jun. 1981.
- [15] I. C. P. S. C.L. Cássio, "The Carnot cycle and the teaching of thermodynamics: a historical approach," *Phys. Educ*, 2016.
- [16] J. Butler, "Carnot's Cycle and the Efficiency of Heat Engines."
- [17] A. N. Singh, "Study of Deformation and Fracture Behaviour of Alloy 617," 2017.
- [18] J. P. Shingledecker, "The US DOE/OCDO A-USC materials technology R&D program," in *Materials for Ultra-Supercritical and Advanced Ultra-Supercritical Power Plants*, Elsevier Inc., 2017, pp. 689–713. doi: 10.1016/B978-0-08-100552-1.00020-8.
- [19] "Special Metals Special Metals, "INCONEL ® alloy 617." Accessed: May 14, 2025. [Online]. Available: [www.specialmetals.com](http://www.specialmetals.com)
- [20] W. E. Frazier, "Metal Additive Manufacturing: A Review.," *JMEP*, pp. 1917–1928, 2014.
- [21] T. et al. DebRoy, "Additive manufacturing of metallic components – Process, structure and properties," *Prog Mater Sci*, 2018.
- [22] D.-G. et al. Ahn, "Characterization of microstructure and hardness of laser clad Inconel 617 superalloy. ," *Surf Coat Technol*, pp. 831–840, 2018.
- [23] Y. , et al. Zhang, "Microstructure and mechanical properties of Inconel 617 fabricated by laser powder bed fusion," 2020.
- [24] M. A. , et al. Jafari, "Process monitoring in laser-based additive manufacturing. ," *Mater Today Proc*, pp. 1533–1538.
- [25] D. , P. N. , & S. B. Pal, "A study of microstructure and microhardness in laser based directed energy deposition of Inconel 617," *Rapid Prototyp J*, 2016.
- [26] B. Avinash, K. M. Subramanian, and V. Rajkumar, "Microstructure, Mechanical Properties and Corrosion Behavior of Inconel 617 Superalloy Fabricated by Wire

Arc Additive Manufacturing,” *J Mater Eng Perform*, vol. 32, no. 14, pp. 6270–6280, Jul. 2023, doi: 10.1007/s11665-022-07571-0.

- [27] T. Hassel and T. Carstensen, “Properties and anisotropy behaviour of a nickel base alloy material produced by robot-based wire and arc additive manufacturing”, doi: 10.1007/s40194-020-00971-7/Published.
- [28] S. Thayumanavan, R. Santhanakrishnan, and T. D. B. Kannan, “Experimental Investigation on Single Pulse MIG Welding of Inconel 617,” *Transactions of the Indian Institute of Metals*, vol. 77, no. 1, pp. 105–117, Jan. 2024, doi: 10.1007/s12666-023-03053-6.
- [29] G. P. Kumar, K. R. Balasubramanian, R. K. Kottala, B. K. Chigilipalli, and K. V. P. Prabhakar, “Prediction of tensile behaviour of hybrid laser arc welded Inconel 617 alloy using machine learning models,” *International Journal on Interactive Design and Manufacturing*, Jan. 2024, doi: 10.1007/s12008-024-01888-x.
- [30] G. Pramod Kumar, K. R. Balasubramanian, K. V. Phani Prabhakar, and M. Cheepu, “Investigation of microstructure, mechanical, and corrosion properties of Inconel 617 joints welded by laser–MIG hybrid welding,” *Proceedings of the Institution of Mechanical Engineers, Part L: Journal of Materials: Design and Applications*, vol. 237, no. 9, pp. 1921–1934, Sep. 2023, doi: 10.1177/14644207231161992.
- [31] I. Jeon, L. Yang, K. Ryu, and H. Sohn, “Online melt pool depth estimation during directed energy deposition using coaxial infrared camera, laser line scanner, and artificial neural network,” *Addit Manuf*, vol. 47, Nov. 2021, doi: 10.1016/j.addma.2021.102295.
- [32] L. Miao, F. Xing, Y. Chai, and L. Miao, “Closed Loop Control of Melt Pool Width in Laser Directed Energy Deposition Process Based on PSO-LQR,” *IEEE Access*, vol. 11, pp. 78170–78181, 2023, doi: 10.1109/ACCESS.2023.3292789.
- [33] Z. Smoqi *et al.*, “Closed-loop control of meltpool temperature in directed energy deposition,” *Mater Des*, vol. 215, Mar. 2022, doi: 10.1016/j.matdes.2022.110508.
- [34] M. Akbari and R. Kovacevic, “Closed loop control of melt pool width in robotized laser powder–directed energy deposition process,” *International Journal of Advanced Manufacturing Technology*, vol. 104, no. 5–8, pp. 2887–2898, Oct. 2019, doi: 10.1007/s00170-019-04195-y.
- [35] A. U. Khan, M. Patidar, and Y. K. Madhukar, “In-Situ Temperature Monitoring and Feedback Control in the Gas Tungsten Arc Welding Process,” *International*

- Journal of Precision Engineering and Manufacturing*, vol. 23, no. 12, pp. 1367–1380, Dec. 2022, doi: 10.1007/s12541-022-00704-4.
- [36] D. Salehi and M. Brandt, “Melt pool temperature control using LabVIEW in Nd:YAG laser blown powder cladding process,” *International Journal of Advanced Manufacturing Technology*, vol. 29, no. 3–4, pp. 273–278, Jun. 2006, doi: 10.1007/s00170-005-2514-3.
  - [37] A. J. Myers *et al.*, “High-resolution melt pool thermal imaging for metals additive manufacturing using the two-color method with a color camera,” *Addit Manuf*, vol. 73, Jul. 2023, doi: 10.1016/j.addma.2023.103663.
  - [38] C. V. Rao, N. C. S. Srinivas, G. V. S. Sastry, and V. Singh, “Dynamic strain aging, deformation and fracture behaviour of the nickel base superalloy Inconel 617,” *Materials Science and Engineering: A*, vol. 742, pp. 44–60, Jan. 2019, doi: 10.1016/j.msea.2018.10.123.
  - [39] C. V. Rao, N. C. S. Srinivas, G. V. S. Sastry, and V. Singh, “Low cycle fatigue, deformation and fracture behaviour of Inconel 617 alloy,” *Materials Science and Engineering: A*, vol. 765, Sep. 2019, doi: 10.1016/j.msea.2019.138286.
  - [40] Q. Wu, T. Mukherjee, A. De, and T. DebRoy, “Residual stresses in wire-arc additive manufacturing – Hierarchy of influential variables,” *Addit Manuf*, vol. 35, Oct. 2020, doi: 10.1016/j.addma.2020.101355.
  - [41] B. Ahmad, X. Zhang, H. Guo, M. E. Fitzpatrick, L. M. S. C. Neto, and S. Williams, “Influence of Deposition Strategies on Residual Stress in Wire + Arc Additive Manufactured Titanium Ti-6Al-4V,” *Metals (Basel)*, vol. 12, no. 2, Feb. 2022, doi: 10.3390/met12020253.
  - [42] C. Liu, Y. Zhan, H. Zhao, S. Shang, and C. Liu, “The Effect of Process Parameters on the Temperature and Stress Fields in Directed Energy Deposition Inconel 690 Alloy,” *Materials*, vol. 17, no. 6, Mar. 2024, doi: 10.3390/ma17061338.